



Master *Photonics for Security Reliability and Safety* (PSRS)



POLITECNICO
DI TORINO

Characterization and Correction of Optical Aberrations in MINFLUX Superresolution Microscopy

Master Thesis Report

Presented by

Francisco Matos Álvarez

and defended at

Université Jean Monnet

August 30th, 2023

Academic Supervisor: Carlo Ricciardi Ph.D.

Host Supervisor: Francisco Balzarotti, Ph.D.

Jury Committee: Carlo Ricciardi, Ph.D, Politecnico di Torino

Ninfa del Carmen Lozano Rincon, Ph.D, Université Jean Monnet

Abstract

The master thesis project was focused on a Python implementation of an indirect sensing adaptive optics algorithm to correct optical aberrations from vortex and top-hat beams, which are beam shapes of interest in the Maximally Informative Luminescence Excitation *MINFLUX* superresolution microscopy technique for imaging and tracking at the subnanometric scale.

The indirect sensing approach involved segmenting the objective lens' entrance into 51 smaller sections using binary masks using a liquid crystal spatial light modulator *LC-SLM*, with each segment having an electric field associated with it. When scanning fluorescent beads, by sequentially intersecting at the focal plane the central electric field of the objective lens with the remaining electric fields from the segments deliberately introducing four phase differences using the *LC-SLM*, four interference patterns were recorded for each combination of central-segment pairs.

The recorded data was processed in a series of steps, including phase unwrapping, polynomial fitting, interpolation, and extrapolation, generating phase maps that would be uploaded into the *LC-SLM* to correct for optical aberrations. Lastly, deliberately inducing controlled aberrations onto the corrected beam profiles with the *LC-SLM* was done to observe astigmatism and trefoil's effect on the beam profiles, individually.

Keywords: Adaptive optics, MINFLUX microscopy, spatial light modulator, optical aberrations

Resumen

El proyecto de tesis de maestría se centró en la implementación en Python de un algoritmo de óptica adaptativa de detección indirecta para corregir aberraciones ópticas de haces de vórtice y de forma de sombrero de copa. Estos haces son de interés en la técnica de microscopía de superresolución de Excitación de Luminescencia Máximamente Informativa *MINFLUX* (por sus siglas en inglés) para la obtención de imágenes y seguimiento a una escala subnanométrica.

El enfoque de detección indirecta implicó segmentar la entrada de la lente del objetivo en 51 secciones más pequeñas utilizando máscaras binarias mediante un modulador espacial de luz de cristal líquido *LC-SLM* (por sus siglas en inglés), con cada segmento con un campo eléctrico asociado. Al escanear cuentas fluorescentes e intersectar secuencialmente en el plano focal el campo eléctrico central de la lente del objetivo con los campos eléctricos restantes de los segmentos, introduciendo deliberadamente cuatro diferencias de fase mediante el *LC-SLM*, se registraron cuatro patrones de interferencia para cada combinación de pares central-segmento.

Los datos registrados fueron procesados en una serie de pasos, que incluyeron desenrollado de fase, ajuste de polinomios, interpolación y extrapolación, generando mapas de fases que se cargarían en el *LC-SLM* para corregir las aberraciones ópticas. Por último, se indujeron deliberadamente aberraciones controladas en los perfiles de haz corregidos con el *LC-SLM* para observar el efecto de astigmatismo y trefoil en los perfiles de haz, de manera individual.

Palabras clave: Óptica adaptativa, microscopía *MINFLUX*, modulador de luz espacial, aberraciones ópticas

Résumé

Le projet de thèse de maîtrise était axé sur une implémentation en Python d'un algorithme d'optique adaptative à détection indirecte pour corriger les aberrations optiques des faisceaux en forme de vortex et de chapeau, qui sont des formes de faisceaux d'intérêt dans la technique de microscopie de super-résolution de Excitation de Luminescence Maximale Informatrice *MINFLUX* (par son acronyme en anglaise) pour l'imagerie et le suivi à l'échelle subnanométrique.

L'approche de détection indirecte impliquait de segmenter l'entrée de l'objectif en 51 sections plus petites à l'aide de masques binaires à l'aide d'un modulateur de lumière spatiale à cristaux liquides *LC-SLM* (par son acronyme en anglaise), chaque segment ayant un champ électrique qui lui est associé. Lors de la numérisation de perles fluorescentes, en intersectant séquentiellement au niveau du plan focal le champ électrique central de l'objectif avec les champs électriques restants provenant des segments, en introduisant délibérément quatre différences de phase à l'aide du *LC-SLM*, quatre motifs d'interférence ont été enregistrés pour chaque combinaison de paires central-segment.

Les données enregistrées ont été traitées en plusieurs étapes, comprenant le dépliage de phase, l'ajustement de polynômes, l'interpolation et l'extrapolation, générant une carte de phase qui serait téléchargée dans le *LC-SLM* pour corriger les aberrations optiques. Enfin, des aberrations contrôlées délibérément induites sur les profils de faisceau corrigés à l'aide du *LC-SLM* ont été réalisées pour observer l'effet de l'astigmatisme et du trèfle sur les profils de faisceau, individuellement.

Mots-clés: Optique adaptative, microscopie *MINFLUX*, modulateur spatial de lumière, aberrations optiques.

Table of Contents

Table of Figures	vii
<i>I. Introduction</i>	1
<i>II. Background</i>	2
II.1. Optical aberrations	2
II.2. Adaptive Optics-Liquid Crystal Spatial Light Modulator	4
II.3. Diffraction-limited resolution	5
II.4. Superresolution Microscopy	7
II.5. MINFLUX	8
II.5.1. MINFLUX 1D localization with two exposures	9
II.5.2. Beam shapes of interest in MINFLUX microscopy	12
II.6. Optical aberrations in MINFLUX 's beam shapes of interest	13
<i>III. Methods</i>	16
III.1. MINFLUX System	16
III.1.1. Optical setup	16
III.1.2. System Lock	17
III.1.3. Measurement control software	18
III.2. Data analysis and simulations software	18
III.3. Optical aberrations correction	18
III.5. PSF measurements	25
<i>IV. Results</i>	26
<i>V. Discussion</i>	34
<i>VI. Bibliography</i>	36

Appendix A - Complementary Information	39
A.1. Generalized MINFLUX statistics	39
A.2. Focus field package calculations	43
A.3. Sample preparation	46
Appendix B - Attributions and Approvals	47
B.1. Copyright clearance for non-self-produced figures	47
B.2. Statement of non-plagiarism	50
B.3. Supervisor approval	51
B.4. Acknowledgement	52

Table of Figures

II.1: Non-normalized Zernike circle polynomials up to the fourth degree	3
II.2: Liquid crystal spatial light modulator's phase modulation	4
II.3: Resolved and unresolved Airy disk patterns	5
II.4: Two PSF separated by the Rayleigh limit	6
II.5: MINFLUX method	9
II.6: MINFLUX in 1D	9
II.7: Probability function for three beam separations L	12
II.8: Vortex beam intensity and phase profiles	13
II.9: Top-hat beam intensity in XZ/YZ and phase profiles	13
II.10: Ideal vortex beam profile in XY and aberrated beam with astigmatism, coma, and trefoil	14
II. 11: Ideal top-hat beam profile and aberrated beam with astigmatism, coma, and trefoil	15
III.1: Schematic of the experimental setup	16
III. 2: Pupil segmentation graph with 51 segments	19
III.3: Central and chosen pupil's electric fields interfering at the focal plane	19
III. 4: Electric field a focal plane	20
III.5: Intensities with different phases applied by the LC-SLM.	20
III. 6: Example of unwrapped phase map for all 50 pupils	22
III.7: Pupil segmentation's Python implementation flowchart	23
III.8: Observed beads with wide-field camera	25
IV.1: Input phase and unwrapped phase maps with its components	26
IV.2: Overall retrieved phase map.	27

IV.3: Retrieved phase without tilt and defocus. -----	27
IV.4: Interpolation map to be uploaded into the SLM. -----	28
IV.5: Intensity profile in XY of vortex beam before and after pupil segmentation correction -----	28
IV.6: Intensity profile of top-hat beam in XY/XZ/YZ before and after pupil segmentation correction -----	29
IV.7: Vortex beam under the influence of applied astigmatism. -----	30
IV.8: Vortex beam under the influence of applied trefoil. -----	30
IV.9: Top-hat beam under the influence of applied astigmatism in XY. -----	31
IV.10: Top-hat beam under the influence of applied astigmatism in XZ. -----	31
IV.11: Top-hat beam under the influence of applied astigmatism in YZ. -----	32
IV.12: Top-hat beam under the influence of applied trefoil in XY. -----	32
IV.13: Top-hat beam under the influence of applied trefoil in XZ. -----	33
IV.14: Top-hat beam under the influence of applied trefoil in YZ. -----	33
A.1: Optical setup in focus field simulations -----	43
A.2: Chamber slide and gold fiducials -----	46

I. Introduction

Recent developments in optical microscopy have greatly improved imaging and tracking at the nanoscale with the goal of further understanding complex biological systems [1] [2]. However, the limitations imposed by optical aberrations and light diffraction still impose a challenge for achieving higher resolution. This has led to the development of adaptive optics *AO* and superresolution microscopy *SRM* techniques that aim to mitigate the effects of aberrations and push the boundaries of resolution beyond the diffraction limit, respectively.

Optical systems can be affected by optical aberrations due to factors like alignment, manufacturing defects, and environmental conditions. These aberrations distort wavefront shapes and have a direct impact on the quality of images produced. Mathematical descriptions of these aberrations are provided by Zernike polynomials [3] [4] and *AO* uses techniques such as indirect wavefront sensing via pupil segmentation to calculate and correct them using *AO* elements like liquid crystal spatial light modulators *LC-SLMs* [5] [6] [7].

On the other hand, *SRM* techniques involves generating distinguishable molecular states within neighboring molecules or target features, typically termed as on and off states. While these techniques share the concept of on/off states, their difference is rooted in how the transition between these states occurs and ascertain the spatial coordinates of a fluorescent emitter or feature [8]. Notably, the innovative Maximally Informative Luminescence Excitation *MINFLUX*.

MINFLUX technique achieves super-resolution through structured excitation patterns instead of relying solely on emitted fluorescence photons. By analyzing the fluorescence from a single emitter under various designed patterns, *MINFLUX* determines the emitter's position based on relative photon counts. This enhances sensitivity, probing near the emitter using patterns with local minima, thus improving photon efficiency [1] [2].

Optical aberrations such as astigmatism, coma, and trefoil, can compromise the quality of data acquisition and overall localization process of the *SRM MINFLUX* technique. The extent of these aberrations can result in variations in the properties of the excitation patterns, potentially causing a decrease in both signal-to-noise ratio and spatial resolution.

Therefore, this master thesis project was focused on implementing a Python routine based on pupil segmentation for optical aberration corrections in a *MINFLUX* system. The method determined phase inconsistencies across the wavefront segments of interest and corrected the aberrated wavefront, improving the quality of the excitation patterns in the system. Additionally, the *LC-SLM* was used to deliberately induce different magnitudes of astigmatism and trefoil onto the corrected beam profiles to observe how the beam shapes of interest were affected.

This thesis begins by defining optical aberrations (II.1), closely tied to limitations in traditional microscopy. It then delves into adaptive optics using *LC-SLM* (II.2), pivotal for compensating for these aberrations. The concept of diffraction-limited resolution is explained (II.3), crucial for pushing imaging boundaries. Subsequent sections introduce *SRM* (II.4) and the innovative *MINFLUX* technique (II.5) with its potential for nanometric resolution. *MINFLUX*'s facets, such as 1D localization and beam shapes (II.5.1 and II.5.2), are detailed, followed by a study of optical aberrations within *MINFLUX* beam shapes of interest (II.6). This sets the groundwork for detailed explanations of specific methods (III), results (IV), and results' discussion (V).

II. Background

II.1. Optical aberrations

Optical imaging systems have many applications in fields such as surveillance, astronomy, medicine, industry, and research and development. At first glance, optical systems appear to produce near-perfect images. However, due to the inherent characteristics of the systems, which include the way optical elements are manufactured and assembled, as well as external factors such as environment and refractive index mismatch, the formed images are not flawless, as they are affected by optical aberrations [3].

Aberrations are commonly described as alterations in the phase of the optical field. These alterations result in deviations from the ideal wavefront shape, such as planar shape for a collimated beam or a spherical shape for a focused beam. Different forms of aberrations emerge due to the interaction of light with a range of internal and external factors [3], including:

- **Astigmatism** arises when an optical system has different focal lengths along two perpendicular axes. This results in a focus appearing as a line along one axis at a certain distance, while at another distance, another focus appears as a line along the other axis.
- **Coma** manifests when the magnification of an optical system varies within the pupil, leading to a distorted focus resembling the shape of a comet's tail.
- **Defocus** occurs when there is a distortion in the focus due to a shifted image plane.
- **Spherical aberration** is characterized by a varying focal length depending on the position within the optical system's pupil.
- **Tilt** refers to the tilting of the overall wavefront along a specific axis.
- **Trefoil** emerges when an optical system introduces irregularities in the wavefront that lead to threefold symmetrical deviations, leading to the characteristic trefoil-shaped pattern.

Each type of optical aberration introduces specific distortions to the captured images, affecting aspects like resolution and contrast. Therefore, understanding how to calculate, compensate, and correct aberrations provides valuable insight into how an optical system operates [3].

The effect of aberrations can be quantified by Zernike polynomials, which represent the complex field in both the exit pupil and the focal plane. Zernike polynomials describe the properties of an aberrated wavefront, regardless of the system's symmetry. These polynomial expressions have many benefits, such as facilitating easy mathematical operations on wavefronts like addition, subtraction, among others. These polynomials form a comprehensive set that permits separation into radial and angular components, and they maintain orthogonality on the unit circle. [4].

Mathematically, Zernike polynomials are expressed as follows [3]:

$$W(\rho, \phi) = \sum_{n=0}^{\infty} \sum_{m=-n}^n a_n^m Z_n^m(\rho, \phi) \quad (\text{II.1})$$

where W represents the wavefront aberrated function, ρ represents the normalized pupil radius, ϕ represents for the angle around the optical axis, and a_n^m stands for the magnitude of the Zernike polynomial $Z_n^m(\rho, \phi)$ with radial order n and azimuthal frequency m . The values of the aberration terms and their classical names, as well as the visual representation of non-normalized Zernike circle polynomials up to the fourth degree, can be seen in Table II.1 and Figure II.1, respectively.

Each Zernike polynomial $Z_n^m(\rho, \phi)$ describes a particular aberration mode with a unique combination of radial and angular dependence. By adjusting the coefficients a_n^m with adaptive optics methods it is possible to simulate and correct for various types and degrees of aberrations in an optical system, thereby improving image quality and overall performance [4].

Table II.1: Zernike polynomials representing the magnitude of optical aberrations, modified from [3] and [4].

#	Order (n)	Frequency (m)	Aberration term	Classical name
1	0	0	1	Piston
2	1	-1	$2\rho \sin \phi$	Tilt (vertical tilt)
3	1	1	$2\rho \cos \phi$	Tilt (horizontal tilt)
4	2	-2	$\sqrt{6}\rho^2 \sin 2\phi$	Oblique astigmatism
5	2	0	$\sqrt{3}(2\rho^2 - 1)$	Defocus (longitudinal position)
6	2	2	$\sqrt{6}\rho^2 \cos 2\phi$	Vertical astigmatism
7	3	-3	$\sqrt{8}\rho^3 \sin 3\phi$	Vertical trefoil
8	3	-1	$\sqrt{8}(3\rho^3 - 2\rho)\sin \phi$	Vertical coma
9	3	1	$\sqrt{8}(3\rho^3 - 2\rho)\cos \phi$	Horizontal coma
10	3	3	$\sqrt{8}\rho^3 \cos 3\phi$	Oblique trefoil
11	4	-4	$\sqrt{10}\rho^4 \sin 4\phi$	Oblique quadrafoil
12	4	-2	$\sqrt{10}(4\rho^4 - 3\rho^2)\sin 2\phi$	Oblique secondary astigmatism
13	4	0	$\sqrt{5}(6\rho^4 - 6\rho^2 + 1)$	Primary spherical
14	4	2	$\sqrt{10}(4\rho^4 - 3\rho^2)\cos 2\phi$	Vertical secondary astigmatism
15	4	4	$\sqrt{10}\rho^4 \cos 4\phi$	Vertical quadrafoil

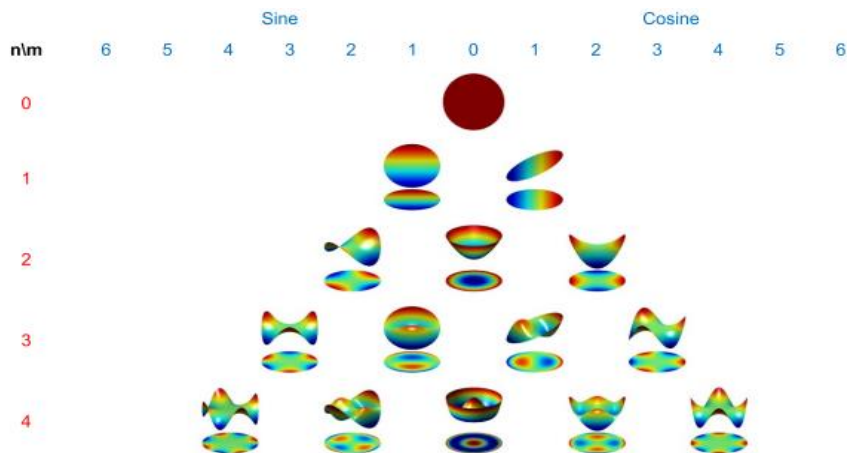


Figure II.1: Non-normalized Zernike circle polynomials up to the fourth degree, modified from [4].

II.2. Adaptive Optics-Liquid Crystal Spatial Light Modulator

Adaptive optics *AO* comprises a set of electro-optical and computational methods designed to alleviate and rectify optical aberrations. By locally modifying the optical field, *AO* aims to reinstate the optimal functioning of an optical system. This approach works to counter the impact of aberrations by introducing a customized wavefront with a phase that offsets the aberrations. Accomplishing this entails the precise evaluation or detection of aberrations to accurately determine the required phase adjustment [5].

Aberration measurement in *AO* systems can be done through direct wavefront sensing or indirect (sensorless) methods. Direct sensing is mainly associated with the Shack-Hartmann sensor, which consists of an array of lenslets and a camera that detects shifts in spot positions to determine local wavefront tilt and aberrations. On the other hand, sensorless *AO* intentionally uses aberrated images to infer the necessary corrections, reducing the need for extensive hardware modifications [6].

Sensing and correction of aberrations can be accomplished using various *AO* elements, including deformable mirrors and spatial light modulators *SLM*. An *SLM* is a two-dimensional dynamically reconfigurable device that enables the modulation of the optical field, intensity, phase, or polarization of an incident beam. A widely employed category of *SLMs* are Liquid crystal spatial light modulators *LC-SLMs*, which take advantage of the electro-optical asymmetry found in liquid crystals. [7].

Liquid crystals *LC* are organic substances possessing distinctive physico-chemical attributes that lie between those of solids and liquids. These substances consist of elongated molecules that display structural and directional properties, resulting in anisotropic attributes in terms of optics, dielectrics, and elasticity. Compared to regular crystals, *LCs* have higher optical anisotropy, typically with an optical birefringence ranging from 0.1 to 0.2. These materials maintain a liquid-like order, allowing fluidity in various *LC* mesophases and providing adjustable properties [7].

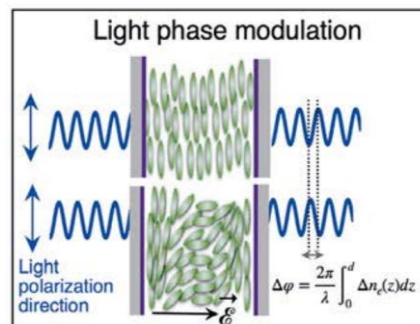


Figure II.2: Liquid crystal spatial light modulator's phase modulation [7].

Applying an electric field \mathcal{E} causes elastic forces to reorient the molecules, minimizing strain energy by aligning them in the direction of the electric field. In liquid crystals exhibiting positive dielectric anisotropy, the state of lowest energy occurs when the molecules align themselves with the electric field. By adjusting the intensity of the electric field, the typical molecular alignment can be changed, resulting in the ability to electronically influence the medium's optical refractive index, denoted as n . As a result, alterations occur in the phase φ of light propagating through the medium at a given wavelength λ [7].

By controlling the spatial arrangement of the electric field applied, either in one or two dimensions, it becomes possible to alter the phase of an incoming optical wave in specific locations. This incident light is termed the "readout beam," with the information intended to be encoded onto its phase carried by the recording signal. To ensure effective manipulation by the LC component, the readout beam's polarization is crucial, as it can govern the parameter that the LC modulates, be it phase, amplitude, or polarization [7].

When linearly polarized light is projected at a 45° angle relative to the extraordinary axis of the LC, it leads to a disparity in phase between the two mutually perpendicular polarized components. This dynamic phase discrepancy facilitates the adjustment of light amplitude when the LC element is positioned between a polarizer and an analyzer. This arrangement also permits the transformation of linear polarization into an elliptical one. As a result, a LC-SLM has the capability to accomplish modulation solely in phase, amplitude, polarization, or a combination of phase and amplitude. This versatility enables novel methodologies in microscopy that go beyond the limitations imposed by diffraction, leading to enhanced resolution [7].

II.3. Diffraction-limited resolution

In the realm of light microscopy, light from an infinitesimally small source can be captured and focused by a lens, which directs light toward the corresponding point on the image plane. However, light cannot be focused onto a single point due to diffraction when light passes through a circular aperture; even with a lens acting as one. Consequently, light waves converge and interfere with a three-dimensional diffraction pattern known as the point spread function *PSF*. The *PSF* is an intensity distribution with a primary maximum at the focal point and progressively weaker maxima distributed symmetrically throughout the three-dimensional volume [8].

The distribution's pattern is known as 'Airy Disk', whose size is inversely proportional to the aperture size and determines the minimal spot size to which a beam can be focused. The quality of the imaging system is characterized by the transmittance of spatial frequencies, therefore, reducing the size of the aperture results in higher frequencies getting excluded from the image formation, which leads to a loss of information and a more spatially extended image [8].

If two point-like sources are focused by a lens with a circular aperture, two Airy disk patterns might be observed on the image plane depending on the distance d between them. When the two main maxima points of each pattern can be distinguishably observed, the diffraction pattern is considered resolved. On the other hand, the diffraction pattern is considered unresolved if the individual patterns merge with each other [8], as seen in Figure II.3.

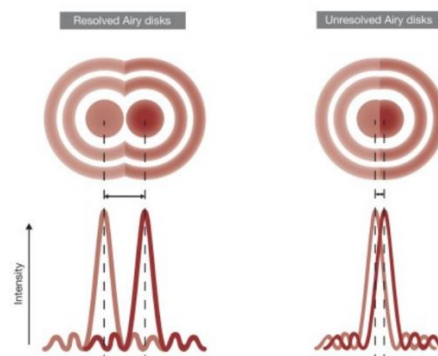


Figure II.3: Resolved and unresolved Airy disk patterns, modified from [9].

In 1883, Ernst Karl Abbe stated that the limit of resolution, i.e. The minimal distance d required for two objects to be resolved, was influenced by the numerical aperture NA of the optical component and the wavelength of light λ being used [8].

$$\sigma = \frac{\lambda}{2NA} \quad (11.2)$$

In the following years, there were continued efforts to improve the precise characterization of resolution limits. For instance, the Rayleigh criterion established that two distinct points could be considered resolved if the peak of the PSF coincided with the first trough of the adjacent PSF . The distance d to this initial intensity minimum is influenced by both the wavelength λ and the NA of the optical system. The NA can be expressed in relation to the lens's focal length f and the aperture D located in front of it ($NA \approx D/2f$) [8].

$$\sigma_{Rayleigh} = 0,61 \frac{\lambda}{NA} \quad (11.3)$$

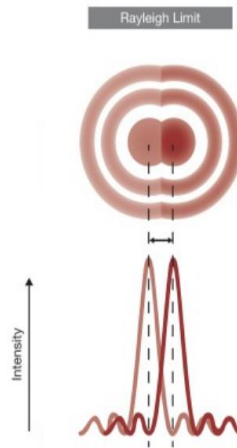


Figure 11.4: Two PSF separated by the Rayleigh limit, modified from [9].

The Airy disk can be estimated using a Gaussian function, where the system's resolution is determined by its Full Width at Half Maximum $FWHM$. Consequently, two distinct points are considered resolved if their separation exceeds the $FWHM$ value. This condition ensures that the trough between the two Airy disks reaches at least 50% of the peak value [8].

$$\sigma_{FWHM} = FWHM = 1,028f \frac{\lambda}{D} \quad (11.4)$$

In terms of NA ,

$$\sigma_{FWHM} = 0,514 \frac{\lambda}{NA} \quad (11.5)$$

The measurement of the PSF with the Airy disk accounts for 86% of the total intensity. As a result, only a small proportion of the total intensity, which is present in the side lobes, is excluded from this definition of

resolution. Despite this omission, the Airy disk is widely utilized in light microscopy as it is readily available [8].

II.4. Superresolution Microscopy

Any optical microscopy method employed to visualize structures smaller than the diffraction-limited resolution of traditional light microscopy ($\sim 250\text{nm}$) is known as a super-resolution microscopy *SRM* technique [10]. The main principle of the *SRM* technique consists of inducing distinct distinguishable molecular states in molecular neighbors or features from the target, often referred to as on and off states. Although these techniques share the common principle of on/off states, they vary in terms of how they achieve the transition between these states and how they determine the spatial position of a fluorescent emitter or feature. Based on the localization process, the *SRM* techniques are divided into coordinate-targeted and coordinate-stochastic super-resolution techniques [11].

The most prominent coordinate-targeted super-resolution techniques are Stimulated Emission Depletion microscopy *STED* [12] and Reversible Saturable Optical Fluorescence Transitions *RESOLFT* [13]. These techniques determine the position of a feature by illuminating it with a specially designed off-switching or on-switching beam. This beam is structured to have at least one local intensity minimum, ideally reaching zero intensity in the focal plane. The precise location of this intensity minimum in the excitation light determines where the molecules are capable of emitting fluorescence [11].

As the position of the intensity minimum is consistently determined using a beam-positioning device, every identified fluorescence photon can be directly attributed to this known and targeted spatial position. Consequently, the source of each detected photon is precisely known, with the level of precision determined by the effective width of the emitter distribution in the *on* state after switching off. In a basic model, the resulting resolution can be expressed as follows [11]:

$$\sigma \approx \frac{\sigma_{PSF}}{\sqrt{1 + I/I_s}} \quad (II.6)$$

Where σ_{PSF} corresponds to the diffraction-limited spot width, I the intensity of the off-switching beam, and I_s the intensity level at which the probability for off-switching is 0.5.

On the other hand, coordinate-stochastic super-resolution techniques such as Photoactivated Localization Microscopy *PALM* [14], Stochastic Optical Reconstruction Microscopy *STORM* [15], and DNA Point Accumulation for Imaging in Nanoscale Topography *DNA-PAINT* [16], involve randomly and stochastically switching individual molecules from an off state to an on state within a given space. By carefully selecting experimental parameters like the illumination scheme and chemical environment, the density of active emitters can be adjusted to achieve an average separation larger than the diffraction limit [11].

Subsequently, the exact position of each molecule in the activated state needs to be ascertained by analyzing the diffused diffraction pattern of fluorescence light, which is recorded by a camera. In the absence of extra sources of interference or pixelation in the detector, the precision of localization is roughly proportional to the count of photons detected, denoted as "N" [11].

$$\sigma \approx \frac{\sigma_{PSF}}{\sqrt{N}} \quad (II.7)$$

In other words, determining the spatial location of each fluorescent molecule requires starting from the diffraction-limited spot, which requires many fluorescence photons for achieving high localization precision. Unfortunately, the number of fluorescence photons emitted by fluorescent proteins or organic fluorophores is limited due to transitions to long-lived dark states or irreversible photo-bleaching [11].

Several strategies have been attempted to increase molecular emissions. These include the development and utilization of specialized fluorophores, anti-bleaching agents, cryogenic temperatures, fluorophore-metal interactions, or the transient binding of fluorogenic labels. These approaches have gradually improved localization precision over time. Nevertheless, these approaches still need to improve the accuracy of localization while operating within a predetermined limit of fluorescence photons [11].

Some strategies have emerged to improve photon efficiency, such as SIMFLUX [17], Repetitive Optical Selective Exposure *ROSE* [18], Structured Illumination Microscopy based Point Localization Estimator *SIMPLE* [19], Modulated Localization Microscopy *ModLoc* [20] and Maximally Informative Luminescence Excitation *MINFLUX* [1].

The *MINFLUX* method [1] introduces an effective strategy for precisely locating individual emitters with a reduced photon count. This method leverages the low intensity point of the excitation light to probe the emitter's position, resulting in a significant decrease in the necessary emitted photons while still attaining the desired level of localization accuracy. *MINFLUX* surpasses camera centroid-based localization methods by enabling the capture of super-resolution images with superior localization precision and spatial resolution. It also allows for enhanced spatiotemporal resolution when tracking individual fluorescent molecules [1].

II.5. MINFLUX

The *MINFLUX* localization technique employs a spatial encoding of the incoming fluorescence excitation light rather than the emitted fluorescence photons. The concept behind *MINFLUX* is to investigate the fluorescence emitted by a single emitter using a series of structured excitation light patterns (referred to as exposures) with varying spatial characteristics. The molecule's position is then determined based on the relative counts of fluorescence photons collected from each exposure [1].

By probing the molecule's position using customized excitation light distributions that feature local minima (ideally zero) at different positions near the emitter, there can be a substantial difference in the emitted fluorescence photons across the various exposures. Consequently, this approach enhances the sensitivity to accurately locate a fluorescent emitter in proximity to the intensity minima. Consequently, one can anticipate enhanced photon efficiency, which translates to the need for fewer fluorescence photons to attain a particular level of localization precision [1].

An approach to create this set of exposures involves utilizing an excitation beam with a localized area of low intensity, such as a doughnut-shaped focal beam known as vortex beam. This beam is then shifted laterally from one exposure to another using a rapid beam scanner. The reason behind selecting this experimental setup is its versatility in generating various excitation beam patterns *EBP* and the potential to be implemented as a scanning microscope with confocal detection to minimize background interference [1].

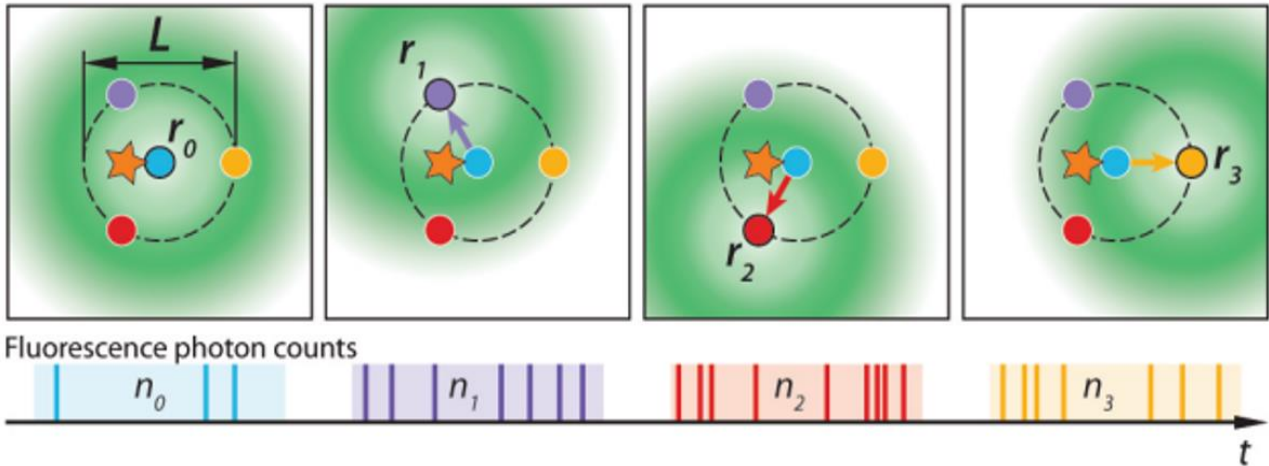


Figure II.5: MINFLUX method: a vortex beam is used to interrogate the emission of an emitter positioned at four different fixed locations. The ratio of photon numbers detected at each position is used to estimate the emitter's localization [1].

The fundamental concept of *MINFLUX* is illustrated using a one-dimensional scenario in the following section. This example highlights the significance of an adjustable geometric parameter that grants complete control over the photon efficiency of the method. Furthermore, it demonstrates that the localization precision achievable with *MINFLUX* can be independent of the wavelength employed in the experiment [1].

II.5.1. MINFLUX 1D localization with two exposures

A fluorescent emitter (represented by a star in Figure II.6) position at x_m along the x -axis can be determined by sequentially analyzing the emitted fluorescence with two excitation light intensity distributions, namely $I_0(x)$ and $I_1(x)$. These distributions exhibit identical spatial characteristics, denoted by $I(x)$, except for a lateral displacement of $\pm L/2$ [21].

$$I_0(x) = I(x - L/2) \tag{II.8}$$

$$I_1(x) = I(x + L/2) \tag{II.9}$$

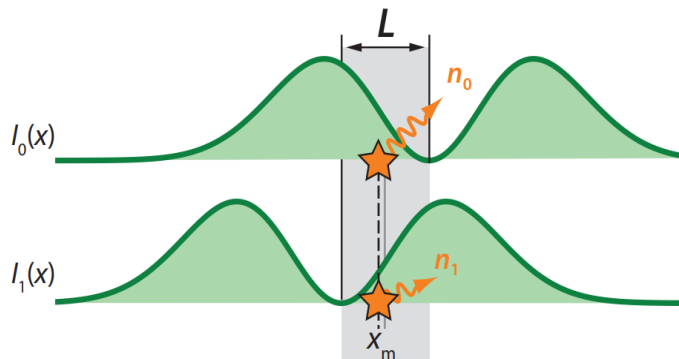


Figure II.6: MINFLUX in 1D: a fluorescent emitter located at x_m probed by two intensity profiles $I_0(x)$ and $I_1(x)$, obtaining two Poisson distributed fluorescence photon count number n_0 and n_1 , respectively [1].

The intensity distribution $I(x)$ may exhibit a minimum intensity at $x = 0$, and it is assumed that the molecule is located between the two probing positions where the excitation light intensity is at its minimum, specifically within the range of $-L/2 < x_m < L/2$. By neglecting background, dark counts, and saturation effects, when probing the molecule using two exposures $I_0(x)$ and $I_1(x)$, it results in two sets of fluorescence photon counts, namely n_0 and n_1 . These counts follow Poisson distributions, with mean values (λ_0 and λ_1) directly proportional to the excitation light intensities at the position of the molecule [21].

$$\lambda_0(x_m) = \alpha I_0(x_m) \quad (II.10)$$

$$\lambda_1(x_m) = \alpha I_1(x_m) \quad (II.11)$$

where $\alpha = c_e q_e \sigma_a$, with c_e as the photon detection efficiency, q_e as the quantum yield of emitter fluorescence, and σ_a as the absorption cross-section of the emitter for the wavelength of the excitation light.

In the scenario of precisely $N = n_0 + n_1$ detected photon counts without any loss of generality, the statistical behavior of n_0 and n_1 , given the total number of N photons, follows the binomial distribution.

$$n_0 \sim \text{Poisson}(\lambda_0), n_1 \sim \text{Poisson}(\lambda_1) \Rightarrow P(n_0|N) \sim \text{Binomial}(n_0, p) \quad (II.12)$$

Where the success probability p is given by

$$p(x_m) = \frac{\lambda_0(x_m)}{\lambda_0(x_m) + \lambda_1(x_m)} = \frac{I_0(x)}{I_0(x) + I_1(x)} =: p_0(x_m) \quad (II.13)$$

Within the range $-L/2 < x_m < L/2$, the condition $0 < p(x_m) < 1$ holds true. As a result, the ratio $p(x_m)/(1-p(x_m))$ is clearly defined as

$$\frac{p(x_m)}{1-p(x_m)} = \frac{\lambda_0(x_m)}{\lambda_1(x_m)} = \frac{I_0(x_m)}{I_1(x_m)} = \frac{p_0(x_m)}{p_1(x_m)} \quad (II.14)$$

with $p_0(x_m)$ defined from equation II.13

$$p_1(x_m) := 1 - p_0(x_m) = \frac{\lambda_1(x_m)}{\lambda_0(x_m) + \lambda_1(x_m)} = \frac{I_1(x)}{I_0(x) + I_1(x)} \quad (II.15)$$

The function $I(x)$ is chosen in such a way that it can be approximated quadratically within the region $-L < x < L$, such that

$$I(x) \approx I_{quad}(x) = \frac{Cx^2}{2} \text{ with concavity } C = \frac{d^2}{dx^2} I(x=0) \quad (II.16)$$

considering equations II.8, II.9, II.14 and II.16

$$\frac{p_0}{p_1} = \left(\frac{x_m - L/2}{x_m + L/2} \right)^2 \quad (II.17)$$

$$\Leftrightarrow \pm \sqrt{\frac{p_0}{p_1}} = 1 - \frac{L}{x_m + L/2} \quad (\text{II.18})$$

$$\Leftrightarrow x_m = L \left(\frac{1}{1 \mp \sqrt{\frac{p_0}{p_1}}} - \frac{1}{2} \right) \quad (\text{II.19})$$

with equation II.19 being restricted by the condition $-L/2 < x_m < L/2$

$$\Leftrightarrow x_m = L \left(\frac{1}{1 + \sqrt{\frac{p_0}{1-p_0}}} - \frac{1}{2} \right) \quad (\text{II.20})$$

In an experimental setup, when a fluorescent emitter is subjected to the two exposures $I_0(x)$ and $I_1(x)$, and a total of N photons are collected, the resulting fluorescent photon counts, n_0 and n_1 , follow a binomial distribution [21]. By analyzing the two photon counts, the success probability p of the binomial distribution can be estimated

$$\hat{p} = \hat{p}_0 = \frac{n_0}{n_0 + n_1} = \frac{n_0}{N} \quad (\text{II.21})$$

Equation II.21 represents the maximum likelihood estimator MLE for the probability p . Using the functional invariance of the MLE along with equations II.20 and II.21, an expression for the molecule location's MLE is derived

$$\hat{x}_m = L \left(\frac{1}{1 + \sqrt{\frac{\hat{p}_0}{1-\hat{p}_0}}} - \frac{1}{2} \right) = L \left(\frac{1}{1 + \sqrt{\frac{n_0}{n_1}}} - \frac{1}{2} \right) \quad (\text{II.22})$$

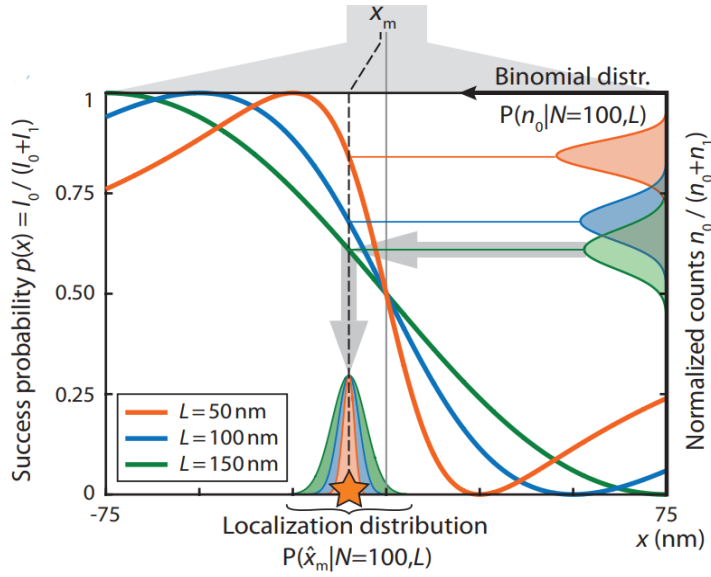


Figure II.7: Probability function for three beam separations L : The binomial distribution behavior of the photon collection probability (equation II.13) is plotted to the right vertical axis as a function of normalized counts for each L . As the value of L is reduced, the width of the distribution decreases as well [1].

The expression in equation II.22 is unaffected by the concavity C of the excitation intensity minimum and exhibits a linear relationship with the beam separation L . Moreover, when the emitter is positioned at the center of the two probing minima ($x_m = 0$), the success probability $p = p_0 = p_1 = 0.5$ remains unaffected by both the beam separation L and the concavity C . Consequently, the distribution of n_0 and n_1 is also independent of L and C . Furthermore, the localization precision σ of \hat{x}_m at $x_m = 0$ scales linearly with L and is not influenced by C [21].

$$\sigma_{\hat{x}_m}(x_m = 0) \propto L \quad (\text{II.23})$$

Thus, the accuracy remains unaffected by variations in the wavelengths of excitation and fluorescence light, being solely controllable by modifying the beam separation L . This is unlike camera-based localization techniques, where accuracy usually shows a roughly linear correlation with the wavelength of the fluorescence light (Equation II.7).

Although certain factors, such as a finite background and imperfections in the beam shape were not considered in this example, the feasibility of achieving adjustable photon efficiency through the implementation of the MINFLUX localization method was illustrated. A complete definition that considers different varying dimensions and numbers of exposures can be found in Appendix A.

II.5.2. Beam shapes of interest in MINFLUX microscopy

As discussed in the previous section, *MINFLUX* microscopy relies on a specialized excitation light distribution with specific characteristics, such as localized minima (preferably zero), positioned near the emitter. Two frequently employed excitation patterns in *MINFLUX* are the vortex beam, which is used for 2D localization, and the top-hat beam, employed for 3D localization.

The vortex beam is characterized by an isochronous surface with helical angular momentum. As it propagates, the beam's center becomes singular due to phase uncertainty or abrupt changes. At this singular point, the intensity is zero, resulting in no heating or diffraction effects. To create the vortex beam, a collimated laser beam can be transformed by applying a spiral phase template onto a grating mounted on an SLM [22].

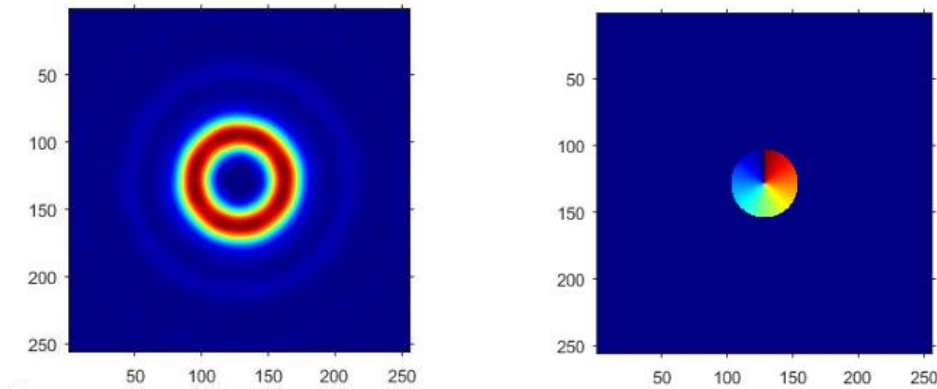


Figure II.8: Vortex beam intensity and phase profiles, respectively [22]

By introducing a different phase mask on the *LC-SLM*, it is possible to generate a top-hat beam profile. The phase alteration in the mask modifies half of the beam's intensity, resulting in destructive interference at the focal point. As a result, two noticeable axial side lobes become apparent both above and below the focal plane when the beam undergoes focusing [23].

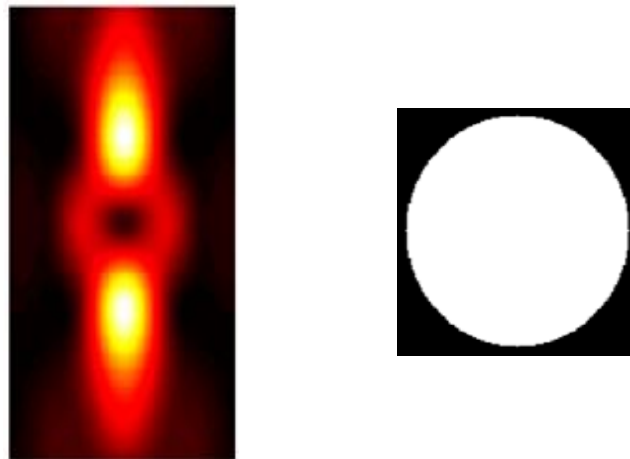


Figure II.9: Top-hat beam intensity in XZ/YZ and phase profiles, respectively [24]

II.6. Optical aberrations in MINFLUX 's beam shapes of interest

The presence of different optical aberrations such as astigmatism, coma, and trefoil can significantly affect characteristics of the beam shapes of interest in *MINFLUX* microscopy, such as the shape itself, the peak intensity, the zero intensity, and the full width at half maximum *FWHM*. These effects compromise the quality of data acquisition and overall localization process during the reconstruction of the final image since the *PSF* is distorted and the fluorescence intensity is diminished, leading to a reduction in both the signal-to-noise ratio, and spatial resolution [25].

Oblique astigmatism introduces a loss of symmetry, resulting in a notable distortion of the pattern structure. This distortion caused the vortex beam to split into two parts, and the central hollow became tilted and stretched. Vertical coma introduces a small displacement in the pattern along the y-direction, resulting in a notable non-uniformity in the intensity. Lastly, the trefoil effect contributes to the formation of a complex, distorted pattern, characterized by a distinctive three-lobe shape. Figure II.10 displays the non-aberrated vortex beam in 400 nm by 400 nm grids along with three of the aforementioned aberrations, each with significant magnitudes, allowing for a clear visualization of their effects.

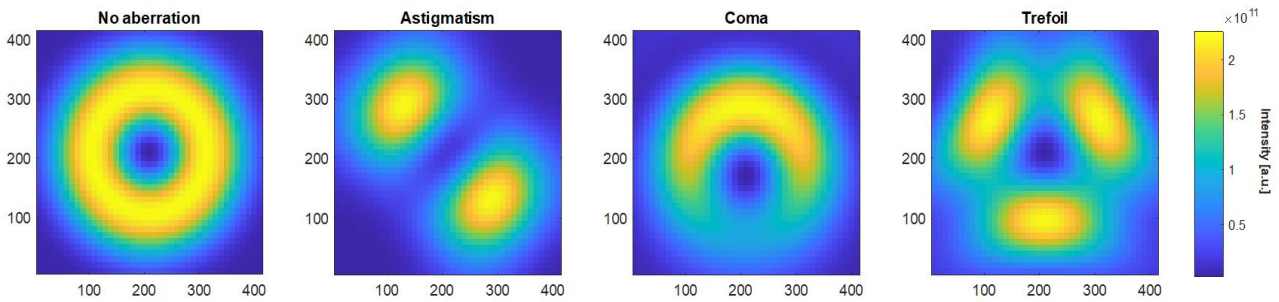


Figure II.10: Ideal vortex beam profile in XY and aberrated beam with astigmatism, coma, and trefoil, respectively [Simulations]

In contrast to the vortex beam, where aberration effects primarily impact localization in the XY plane (along the optical axis) for 2D applications, the top-hat profile requires comprehensive analysis across the XY, as well as the XZ and YZ planes (perpendicular to the optical axis) due to its application in 3D localization; the top-hat beam profiles under the effect of the mentioned aberrations are shown in 400 nm by 400 nm grids in Figure II.11.

In the XY plane, oblique astigmatism can cause the top-hat profile to appear elliptical, with different radii in the x and y directions. The elliptical shape will have major and minor axes, indicating the varying focal lengths along those directions. In the XZ and YZ planes, astigmatism will make the intensity profile appear elongated along the Y and X axis, respectively.

Vertical coma affects the top-hat profile primarily in the XY and YZ planes, causing an asymmetric distortion along the X-axis in both planes. In the XZ plane, the top-hat profile remains relatively unaffected and maintains its uniform distribution across the width.

On the other hand, trefoil along x will cause the top-hat profile to have three lobes in the XY and XZ planes (trefoil along x case), creating triangular-like intensity distributions just as in the case of the vortex beam. However, trefoil will not have a significant effect on the YZ plane, keeping the intensity distribution unaffected.

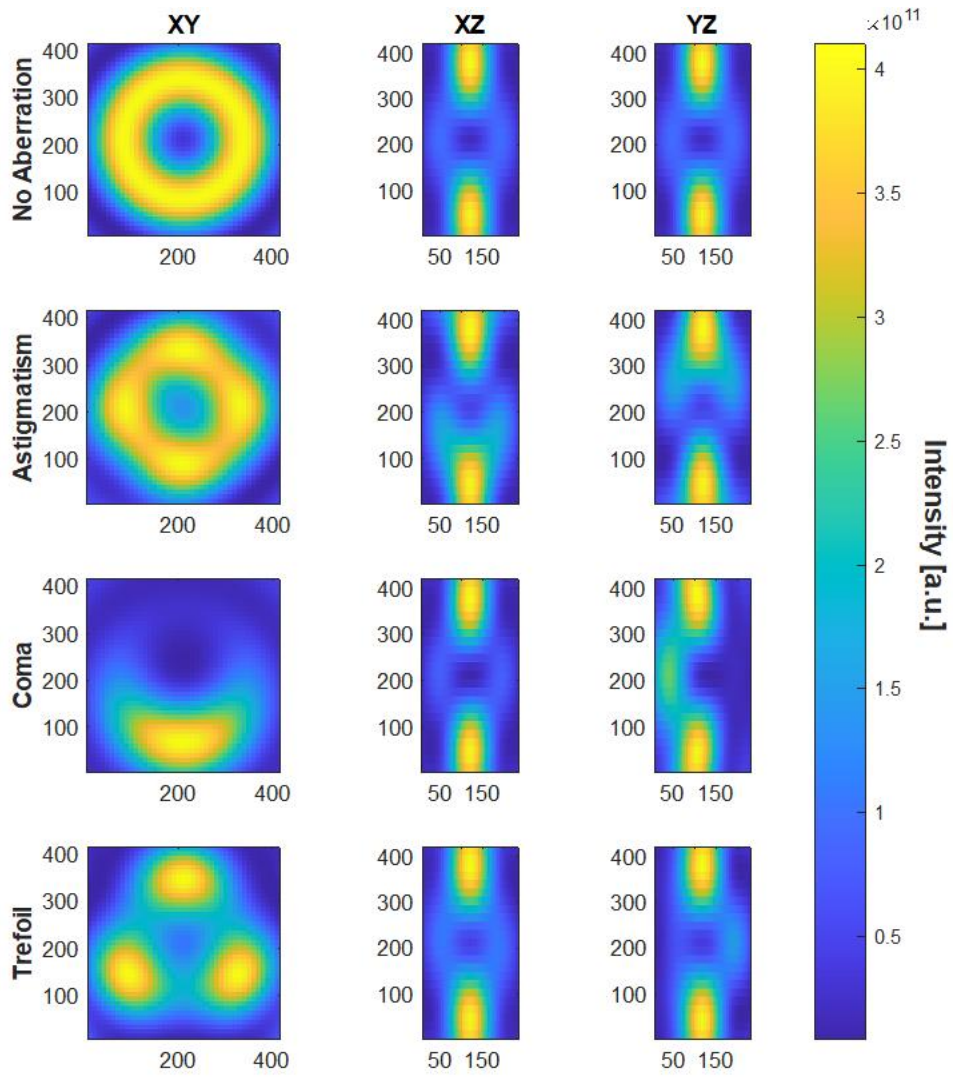


Figure II. 11: Ideal top-hat beam profile and aberrated beam with astigmatism, coma, and trefoil, respectively [Simulations]

III. Methods

In this section, the procedures and tools employed in this master project are detailed. This includes a description of the *MINFLUX* system setup (III.1), encompassing the electro-optical system (III.1.1) with its system locking (III.1.2), and the measurement control software (III.1.3). The data analysis and simulation software are mentioned (III.2), followed by an explanation of the of optical aberrations correction method (III.3) and its Python's implementation (III.4), and elaborating upon the *PSF* measurements for characterizing individual aberration effects (III.5).

III.1. MINFLUX System

The experimental setup entails a specially constructed scanning microscope equipped with swift beam scanning and modulation functionalities, which is a replica of the system used in [1]. A schematic representation of this configuration is presented in Figure III.1. It is worth mentioning that only the measurements pertaining to *PSF* evaluations were conducted in alignment with the thesis project's scope; the full description of the system for the imaging and tracking capabilities can be found in [1].

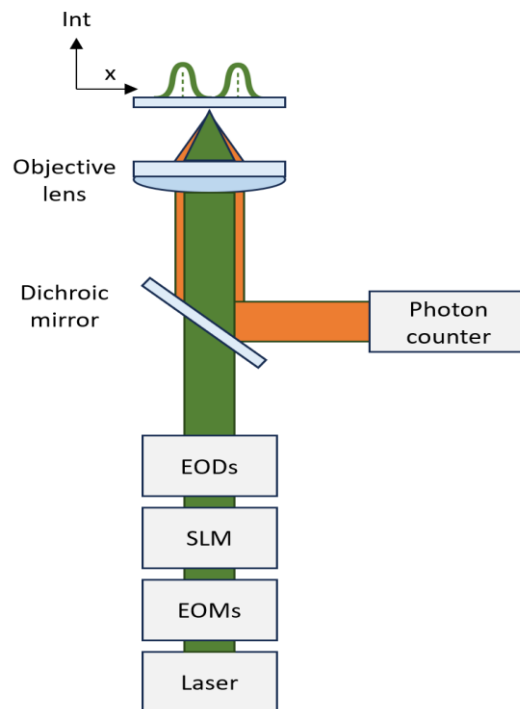


Figure III.1: Schematic of the experimental setup

III.1.1. Optical setup

Built upon the foundation of fluorescence confocal microscopy, *MINFLUX* is a cutting-edge fluorescence confocal microscope designed with modulated excitation [1]. Sample excitation can be achieved using either a vortex beam, a top-hat beam, or through wide-field illumination. The system is equipped with two main lasers operating at wavelengths of 560 nm and 642 nm, respectively. Amplitude modulation and the transition between vortex and top-hat beams are executed through electro-optical modulators *EOMs*. To

achieve beam shaping and correct optical aberrations, a 1920 x 1152 Phase Series spatial light modulator *LC-SLM* produced by Meadowlark Optics is employed.

The lateral scanning of the beam's position across the sample is accomplished through a configuration involving two perpendicular electro-optical deflectors (*EODs*) in conjunction with a piezoelectric tip/tilt mirror. These *EODs* are differentially operated using a pair of high-voltage amplifiers. The first amplifier enables scanning with a bandwidth of 5 MHz, while the second provides scanning capabilities at a bandwidth of 125 kHz. In synergy with the piezoelectric tip-tilt mirror, this setup constitutes a high-dynamic range beam scanning system, facilitating scans across an approximate area of $20 \times 20 \mu\text{m}^2$. Notably, the faster and slower amplifiers offer scanning ranges of approximately $\pm 150 \text{ nm}$ and $\pm 1 \mu\text{m}$, respectively. For precise three-dimensional positioning, the sample is situated on a piezoelectric stage.

The excitation beam pattern *EBP* is multiplexed using the *EODs* and the swift amplifiers. The feedback control mechanism is a combination of *EODs* managed by the gradual controller and the piezoelectric tip-tilt mirror. All scanning devices, comprising the *EODs* and the piezoelectric tip-tilt mirror, are overseen by a field-programmable gate array *FPGA* board.

Laser beams are directed onto the sample via an oil immersion microscope objective. Fluorescence photons are then separated from the excitation light using a dichroic mirror *DC*. A set of mirrors and telescopes (the later to accomplish right magnification between sample plane and detector plane), direct the fluorescent light into a camera or two Avalanche Photodiodes *APDs*. For detection, the *APDs* are linked to a single multimode fiber, whose cores act as spatial filtering detection pinhole with effective size of 600nm. A mirror on a motorized flip mount is used to switch between the camera and the *APDs*.

Besides the excitation lasers, three additional lasers (640, 560 and 488nm) are accessible for illuminating the sample either in a wide-field or focused manner.

To ensure precise spectral filtering when necessary, the lasers in the setup are accompanied by dichroic clean-up filters. Moreover, polarizers and waveplates are integrated to achieve the appropriate polarization for specific experimental conditions.

III.1.2. System Lock

The system is equipped with an integrated lock that continuously supervises and corrects any shifts in the sample's position along all three dimensions.

For evaluating the axial position of the sample, a technique based on measuring displacements of a beam subject to total internal reflection *TIR* at the interface of the coverslip and media is employed. This method involves focusing an infrared laser beam off-center into the objective lens's back focal plane to generate the *TIR* signal. Subsequently, a complementary metal-oxide-semiconductor *CMOS* camera detects this signal, and the center of mass within the camera image serves as an indicator for the axial sample position.

To determine the lateral sample position, a darkfield imaging approach is utilized, whereby nanoparticles are dispersed onto a secondary *CMOS* camera. The nanoparticles' image is fitted with a 2D Gaussian function, and the center position of this function is used as a reference for the lateral sample position.

To ensure consistent axial and lateral sample positions during experiments, a proportional-integral *PI* feedback loop, managed by LabView, commands the xyz piezo stage. The second camera records images at

an approximate frame rate of 90 fps, while camera 3 operates around 160 fps. The acquired images undergo exponential averaging, and the stage's position is updated every 100 ms.

III.1.3. Measurement control software

Custom LabView programs [26] serve a multitude of essential functions, including the control of the FPGA board, the control of laser beam positioning and modulation, the multiplexing of the *EBP*, control of the *SLM*, switching to WF camera, capturing counts from the *APDs*, implementing real-time position estimation via the modified Levenberg-Marquardt algorithm *mLMSE*, and preserving the recorded data.

III.2. Data analysis and simulations software

Data analysis and simulations were performed using *MATLAB* [28] student license 40966311, provided by the Université Jean Monnet. In addition, the *Python* programming language [29] was also used for its versatility and open-access nature, with computations conducted in the Integrated Development Environment (IDE) *VS Code* [30]. Throughout the analysis, a range of *Python* packages were imported such as *NumPy* for numerical computations, *os* for managing operating system-related functionalities, *matplotlib.pyplot* for data visualization, among others.

Additionally, a private *Python* package named *focusfield* developed by the Balzarotti Lab at The Research Institute of Molecular Pathology in Vienna was used to calculate the electric field for high NA focusing scenarios and the effect of Zernike terms in aforementioned field in section II.6. The package is based on reference [31] and it is detailed in Appendix A.

III.3. Optical aberrations correction

As mentioned in section II, the analysis of phase inconsistencies across various segments of the wavefront becomes crucial, especially for the beam shapes of interest in MINFLUX microscopy. Therefore, an indirect sensing approach for addressing optical aberrations correction is chosen, rooted in the methodology outlined in reference [32] based on pupil segmentation, with the distinction that the Point Spread Function (PSF) was captured with the *APDs* relying on fluorescence-based detection rather than using a camera.

In this method, small apertures, known as subpupils, are introduced onto the back focal plane of the objective lens. These subpupils are created on the back focal plane by projecting specific masks from the *LC-SLM* plane using a set of relays/telescopes. It's important to note that the system comprises a single *LC-SLM* that serves a dual purpose – hosting a blazed grating pattern and binary masks.

The blazed grating plays a crucial role in the separation of modulated and non-modulated components. The direct reflection (0^{th} diffraction order), which remains unmodulated by the *LC-SLM*, is blocked using an aperture. On the other hand, the binary masks define the segmented beams, or subpupils. A binary mask operates in a binary fashion, either allowing light to pass through or blocking it. By activating a specific pair of subpupils (the central segment and an offset segment), the binary masks on the *LC-SLM* allow the incoming light only through these designated regions, blocking out the rest.

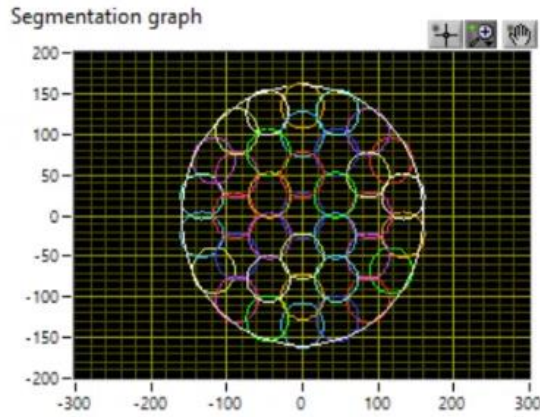


Figure III. 2: Pupil segmentation graph with 51 segments

At the focal plane, paired subpupils are focused and imaged by the objective lens. Analyzing the distribution of light at the point of interference provides the necessary insights for identifying the required wavefront corrections. The smaller the pupil, the better the resolution of the measurement, hence better correction. However, the signal decreases. Additionally, if the pupil is too small, diffraction at the pupil edges becomes more and more apparent. The number of pupils and the spatial distribution depicted in Figure III.2 were chosen as a right trade-off between resolution of the measurement and amount of signal and artifacts due to diffraction.

In the chosen pupil segmentation methodology, the central field is subjected to interference with the remaining number of chosen segments ($N=50$), sequentially (Figure III.3). This involves scanning a fluorescent bead across the field, whose magnitude is given by

$$\vec{E}_f(x, y, z, t) = \vec{E}_{f1}(x', y', z, t) + \vec{E}_{f2}(x', y', z, t) = \vec{E}_{f1}(x, y, z, t)e^{i\omega t} + \vec{E}_{f2}(x, y, z, t)e^{i\omega t + \varphi} \quad (\text{III.1})$$

where the first section (x', y') represents the chosen input fields from the SLM, the second section (x, y) represents the fields at the focal plane and φ represents the phase delay between fields that needs to be compensated to obtain the corrected wavefront.

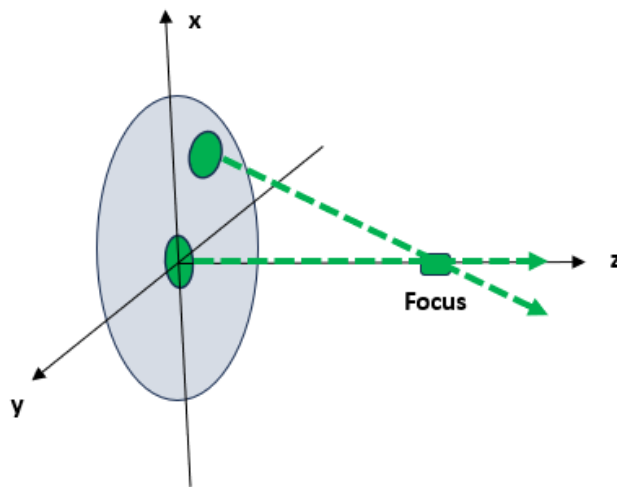


Figure III.3: Central and chosen pupil's electric fields interfering at the focal plane

The electric field described in equation III.1 is a vector that can be represented in a complex plane, illustrated in Figure III.4.a for its x-component. Over time, this field undergoes oscillation, with its intensity denoted by the modulus $|E_f|^2$. The time-averaged intensity of the field is a constant, representing the mean of a Poisson distribution for photon arrival at a specific pixel, as shown in Figure III.4.b.

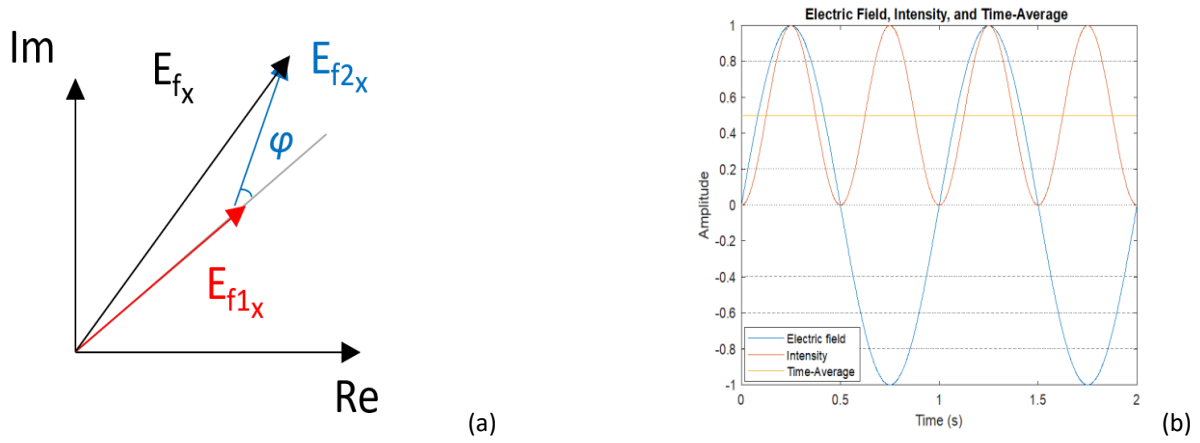


Figure III. 4: Electric field a focal plane (a) x-component in the complex plane (b) oscillating field (red), intensity (blue), time-average (yellow)

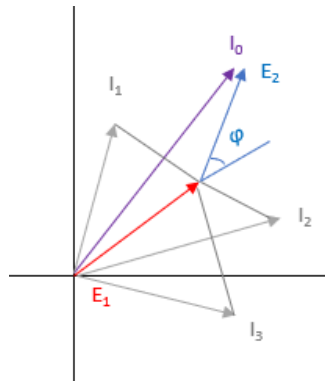


Figure III.5: Intensities with different phases applied by the LC-SLM.

$$I_i = a + b \cos \varphi \quad (\text{III.2})$$

$$I_0 = a + b \cos \varphi \quad (\text{III.3})$$

$$I_1 = a - b \sin \varphi \quad (\text{III.4})$$

$$I_2 = a - b \cos \varphi \quad (\text{III.5})$$

$$I_3 = a + b \sin \varphi \quad (\text{III.6})$$

From the four intensity values, basic trigonometry can be applied to then determine the vertical offset or the DC component of the signal (denoted as a), the amplitude of the cosine function (denoted as b), and the phase difference of interest φ (Equations III.7-9)

$$a = \frac{I_0 + I_2}{2} = \frac{I_3 + I_1}{2} \quad (\text{III.7})$$

$$b = \frac{I_0 - I_2}{2 \cos \varphi} = \frac{I_3 - I_1}{2 \sin \varphi} \quad (\text{III.8})$$

Using the *LC-SLM*, one can add or subtract a delay to the phase of the electric field relative to the central position to measure different intensity values (Equation III.2) which allows one to determine the original phase difference and hence the needed wavefront correction. In the chosen methodology, four intensity values (Equations III.3-6) with different phases were recorded $[0, \pi/2, \pi, 3\pi/2]$, meaning that four images would be captured by each combination of the central segment with the other segments into a HDF5 file (Hierarchical Data Format, Version 5), which is the chosen file type for the *MINFLUX* system in the Balzarotti Lab.

$$\tan \varphi = \frac{I_3 - I_1}{I_0 - I_2} \quad (\text{III.9})$$

The obtained values of the phase difference φ create a phase map for each pair of pupils that can exhibit discontinuities beyond the range of π , requiring a process called phase unwrapping. During phase unwrapping, any 2π jumps are treated as if they did not occur relative to a pixel in the phase map (usually the central one) whose phase is kept constant. Then, the unwrapped phase map is fitted to a 1st order polynomial in two dimensions to obtain contour lines which allows to assess if the results resemble a plane. Additionally, outliers can be determined and then excluded further in the analysis.

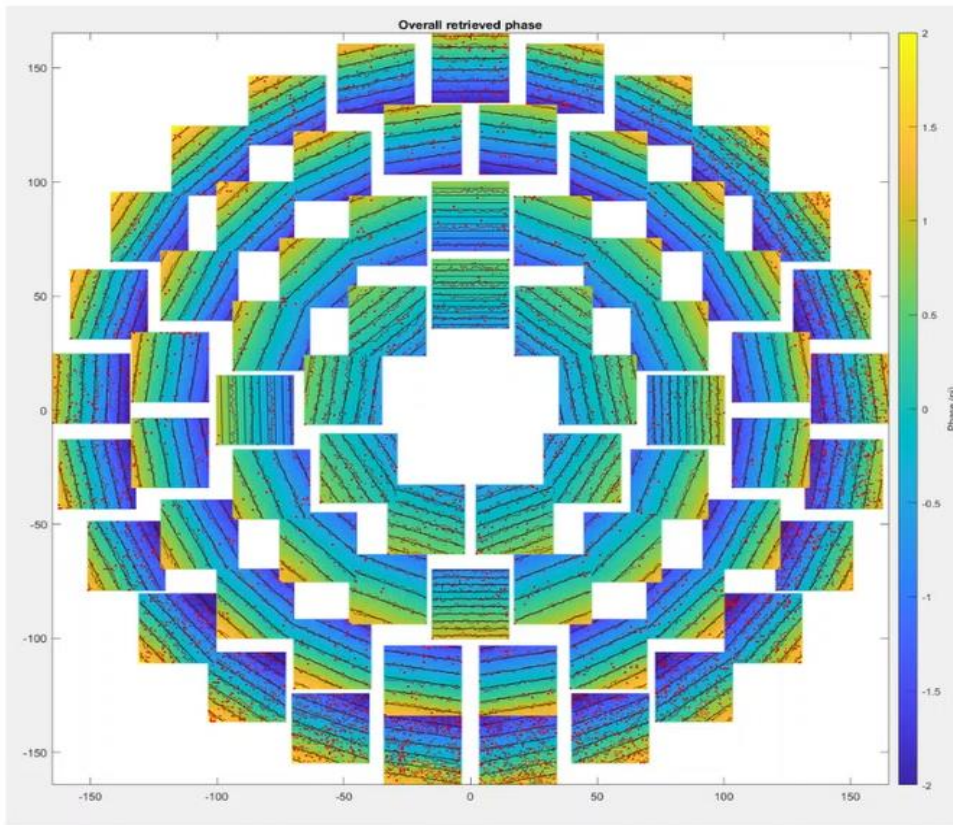


Figure III. 6: Example of unwrapped phase map for all 50 pupils

Then, in each unwrapped phase map for each pupil the central pixel phase relative to the center pupil will be subtracted by a linear fit of the tilt and by a quadratic term of the defocus in the pupil space. With the newly obtained values, an interpolation method can be applied to get the correction in the entirety of the unwrapped phase map, which can then be uploaded to the SLM to correct the aberrated wavefront. It is worth mentioning that extrapolation becomes necessary for the outer pupils that might have part of them outside of the pupil radius.

III.4. Pupil segmentation's Python implementation

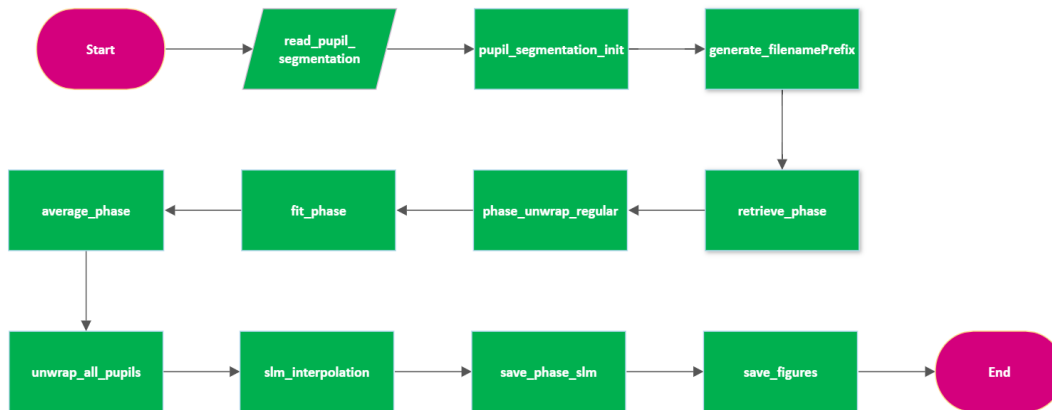


Figure III.7: Pupil segmentation's Python implementation flowchart

Figure III.7 shows the flowchart detailing the pupil segmentation methodology employed using Python to obtain the data presented in the results section. This approach is built upon the approach explained in section III.4 Optical aberrations corrections. Subsequently, the role of each section of the implementation is detailed after the input HDF5 file with the four images by each pupil is provided.

- *read_pupil_segmentation*

Extracts the name and directory location of the input file to construct a full file path and proceeds to open the file with the `h5py.File` function. A Python dictionary named *data* is initialized with the information corresponding to the parameters used during acquisition, the images, and coordinates.

- *pupil_segmentation_init*

The function is initialized by the *data* extracted from the previous function and initializes two new dictionaries named *param* and *out*. The new dictionaries will contain information that controls the steps such as image processing, interpolation, unwrapping, and saving options.

- *generate_filename_Prefix*

Creates a descriptive filename prefix by combining information about the interpolation method, average method, cut method, and zero minimum condition. This prefix is used to generate meaningful filenames when saving output files related to pupil segmentation, making it easier to identify the processing settings used.

- *retrieve_phase*

Extracts various parameters and data arrays from the input dictionary *data*. These parameters include the reference point for phase calculation, the image data, the x and y coordinates of the measurement points, the pre-known phases, and the number of phases used per pupil. Then, the function proceeds to calculate the raw phase for each pupil and then applies the phase unwrapping procedure explained in

the next function. The values of the a and b are determined as well, plot along the unwrapped phase maps and all stored in the *out* dictionary.

- *phase_unwrap_regular*

Applies the *unwrap* function from the *Numpy* library to remove the discontinuities caused by phase wrapping in the raw phase maps. The difference between wrapped and unwrapped phases is determined to determine the phase offset based on a specified pixel location. The offset is then subtracted from the unwrapped phase and returned to the *retrieve_phase* function.

- *fit_phase*

Starts by extracting information from the input dictionaries *data*, *param*, and *out*. Then proceeds to calculate and fit a 1st order polynomial ($a+bx+cy$) from the unwrapped phase maps to determine a median absolute deviation criterion. The values outside the criterion (outliers) are discarded and the polynomial is fit again to obtain new coefficients with the point that were kept.

As a visual aid, plots of the previous calculations for a single pupil and the overall retrieved phase are displayed. Lastly, the calculated phase fit, points to keep, polynomial fit coefficients, and phase with the linear term subtracted are added to the *out* dictionary.

- *average_phase*

Retrieves the phase fit data from the *out* dictionary and calculates the average phase values for each pupil and stored them in the same dictionary.

- *unwrap_all_pupils*

Calculates the tilt of the phase using a 1st order polynomial to x and y coordinates and subtracts it from the average phase values. It then calculates and subtracts a defocus term using a 2nd order polynomial ($a + b * (x^2 + y^2)$). The calculated values after removing tilt and defocus are added to the *out* dictionary.

- *slm_interpolation*

Creates a mesh grid representing the SLM using the information obtained from the previous functions and performs phase interpolation using the thin plate smoothing spline, considering phase values outside the circular region of interest to be extrapolated or set to a constant value to avoid discontinuities near the edges of the region. The retrieve phase structure, the phase without tilt, the phase without defocus, and the interpolation are plotted. Finally, the phase values after the function processing are stored in the *out* dictionary to then be uploaded on the SLM for optical aberrations correction.

- *save_phase_slm*

Converts the phase data from units of π into radians and saves it, along with the associated parameters, into a HDF5 file in the same directory as the input file.

- *save_figures*

Saves the figures generated during the execution of the Python implementation in the same directory as the input file as separate PNG files.

The full code implementation can be found in the GitHub link:

<https://github.com/Franzmats/Optical-Aberration-Corrections.git>

III.5. PSF measurements

A sample with TetraSpeck beads was mounted in the system stage and positioned under *WF* illumination (refer to Appendix A for sample preparation based on [27]). Using the *WF* camera, the beads were observed and some of them were selected, as seen in Figure III.8. The tip/tilt mirror then sent the beams to the selected beads for the *PSF* measurements once the detection was changed from the *WF* camera to the *APD* with the mirror in a motorized flip mount.

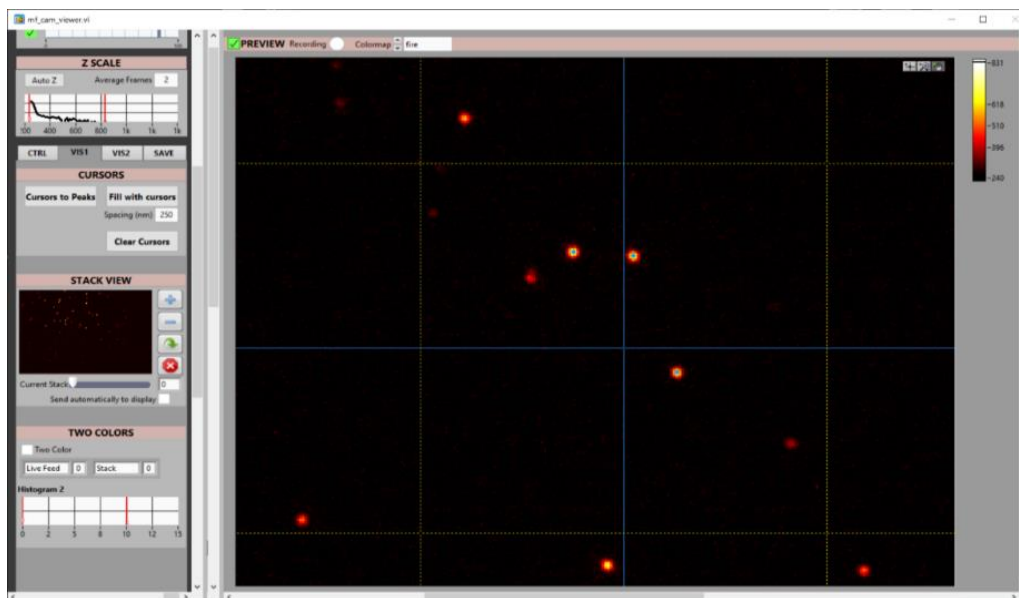


Figure III.8: Observed beads with wide-field camera

The Impector software [33] was used to monitor and record the detected fluorescence in the XY, XZ and YZ planes. The fine stage was used to center the profiles as much as possible, to define a z lock position and then a xy lock position. The lock positions were used to actively stabilize the system after each *PSF* measurement. Then, by manually inputting aberrations on the *LC-SLM* phase map after the correction was done, a set of images under the effect of astigmatism and trefoil were recorded. It is worth mentioning that the collected scans in XY were 80x80 pixels and in XZ/YZ were 80x150 pixels with a pixel size of 10nm.

IV. Results

As mentioned in the Methods section, the *MINFLUX* system was set to scan and interfere the electric field of each of the 50 pupil segments four times with the central pupil's field, recording a total of 200 images. Once the collecting process was done, the pupil segmentation routine was implemented. Figure IV.1 displays the retrieved phase map for each pupil segments in the four chose phase configurations $[0, \pi/2, \pi, 3\pi/2]$, the unwrapped phase map of the pupils (bottom left), the components a and b of each intensity combination and χ as the contrast between the bright and dark regions of the interferometric patterns.

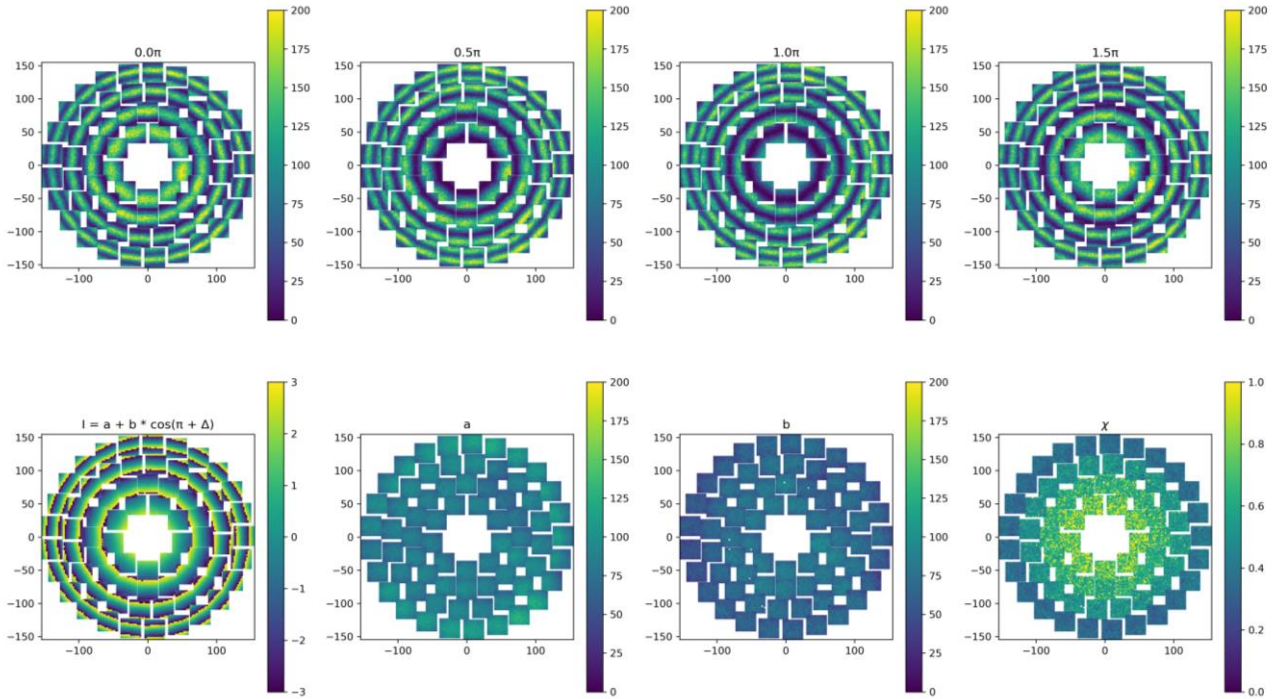


Figure IV.1: Input phase and unwrapped phase maps with its components

Figure IV.2 shows the unwrapped phase maps with fitted phase contour black lines from the 1st order polynomial on top of the unwrapped phase contour red lines to visually assess how well the fitted polynomial represented the actual phase data.

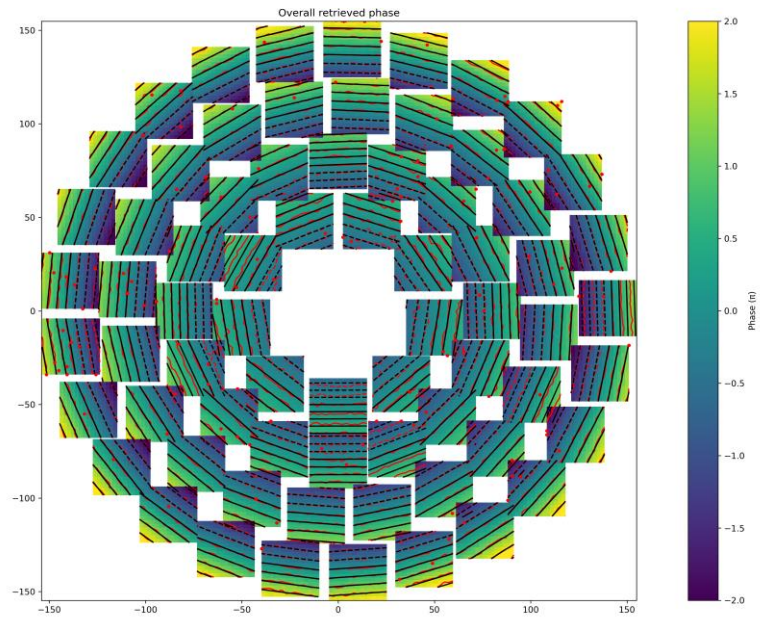


Figure IV.2: Overall retrieved phase map.

The tilt and defocus were determined and subtracted from the phase average of each pupil using 1st and 2nd order polynomials, respectively, as seen in Figure IV.3. Then, the thin plate smoothing spline interpolation method was used to interpolate the phase values after subtracting the polynomials to obtain the interpolated phase values in a grid representing the *LC-SLM* as seen in Figure IV.4. Lastly, the phase values were extrapolated for values outside the circular region, which provided the data that enabled the wavefront correction.

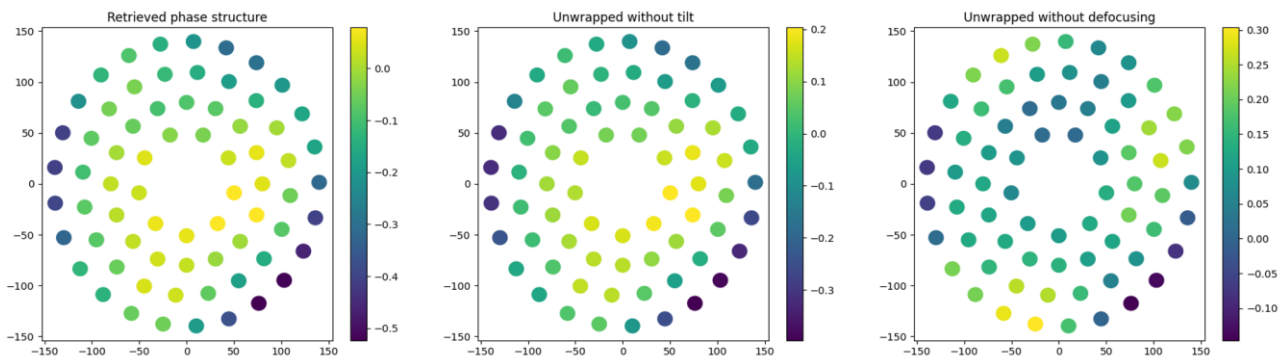


Figure IV.3: Retrieved phase without tilt and defocus.

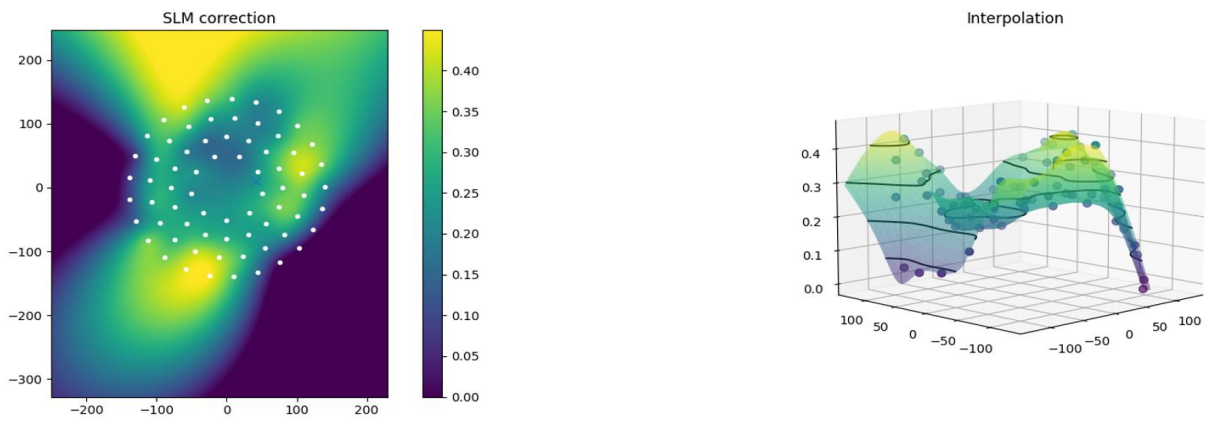


Figure IV.4: Interpolation map to be uploaded into the SLM.

The Python routine was repeated for each segment of the *LC-SLM* that produces a beam shape of interest. Once the routine was completed, the phase information for each segment was uploaded into the *LC-SLM* to correct optical aberrations in the wavefronts, improving the shape of both vortex and top-hat profiles, as seen in Figure IV.5 and Figure IV.6, respectively.

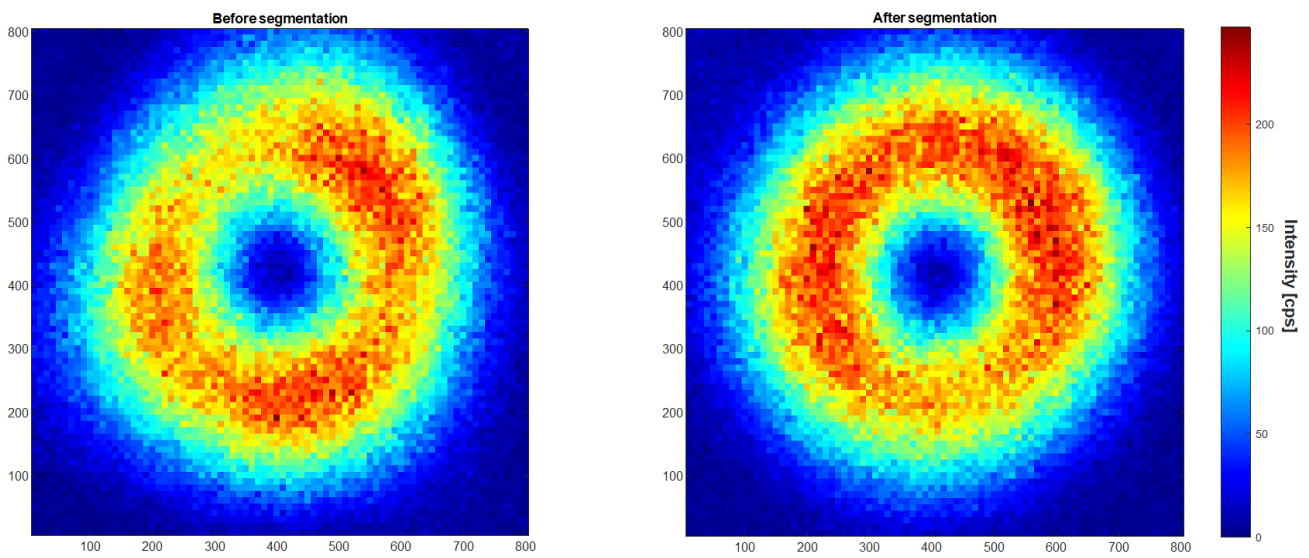


Figure IV.5: Intensity profile in XY of vortex beam before and after pupil segmentation correction

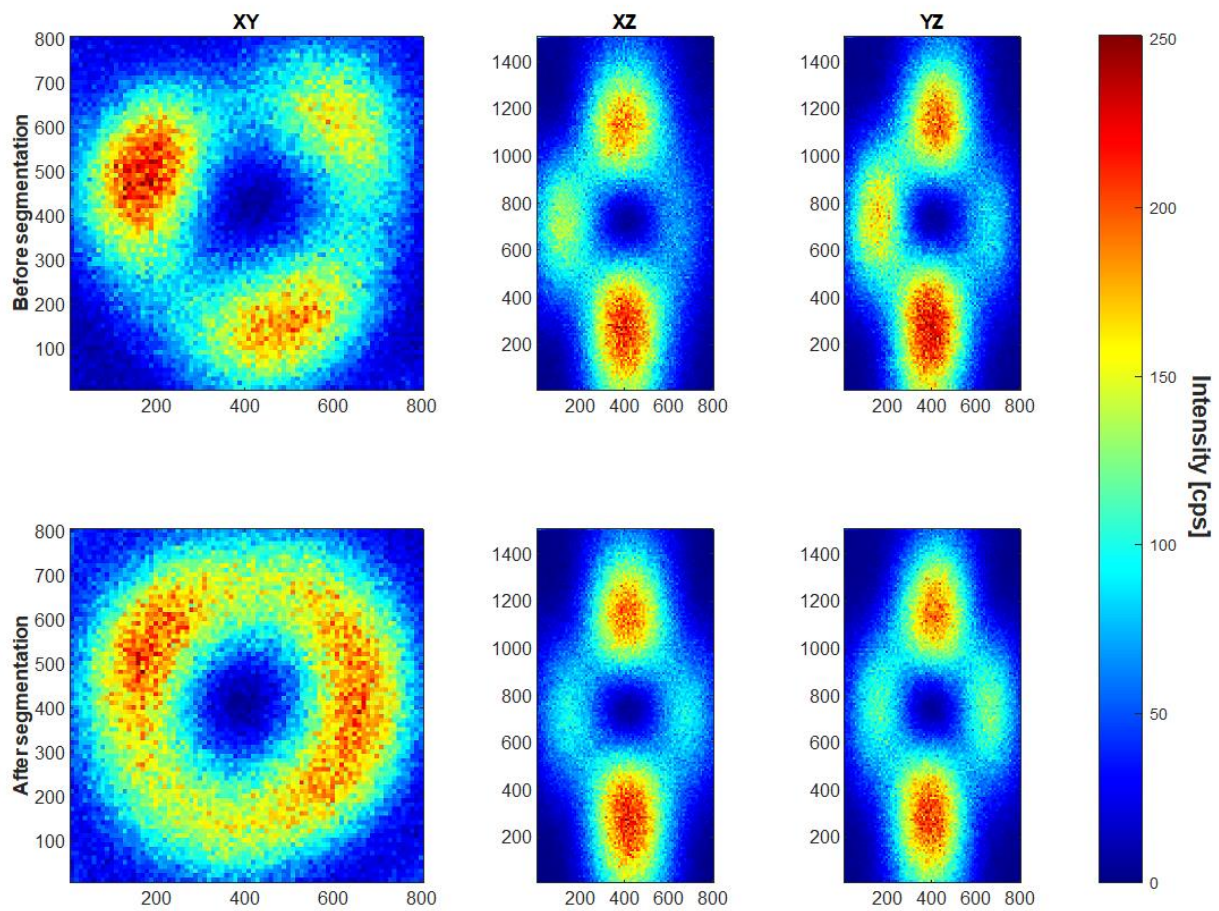


Figure IV.6: Intensity profile of top-hat beam in XY/XZ/YZ before and after pupil segmentation correction

In addition to the wavefront correction, the *LC-SLM* was used to deliberately induce controlled optical aberration's magnitude (adimensional) onto the vortex and top-hat beam profiles, as seen in Figures IV.7-14. This approach provided valuable insights into how deliberate aberrations, namely astigmatism and trefoil, interact with beam shapes of interest in *MINFLUX* microscopy.

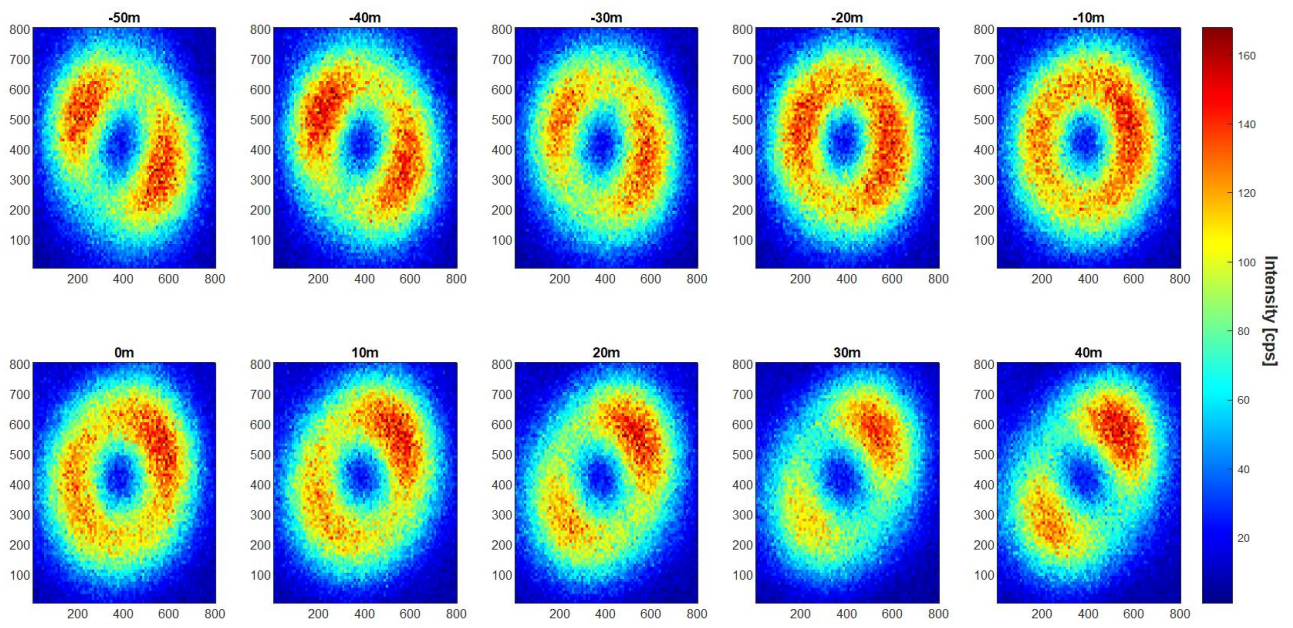


Figure IV.7: Vortex beam under the influence of applied astigmatism.

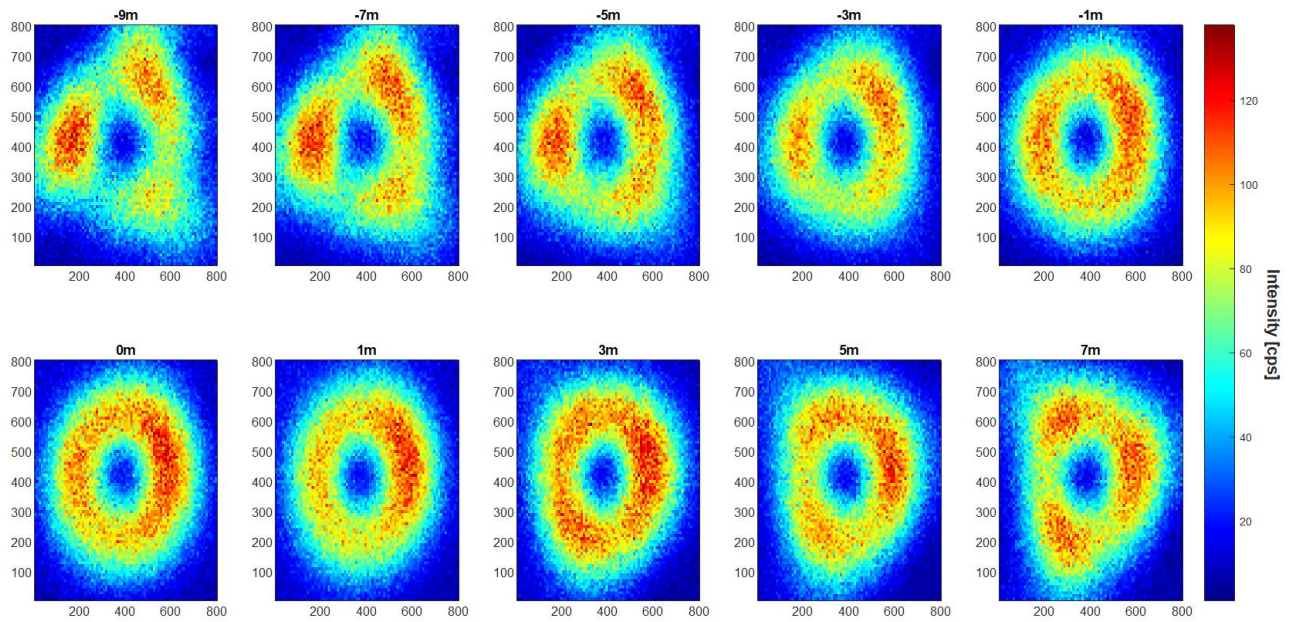


Figure IV.8: Vortex beam under the influence of applied trefoil.

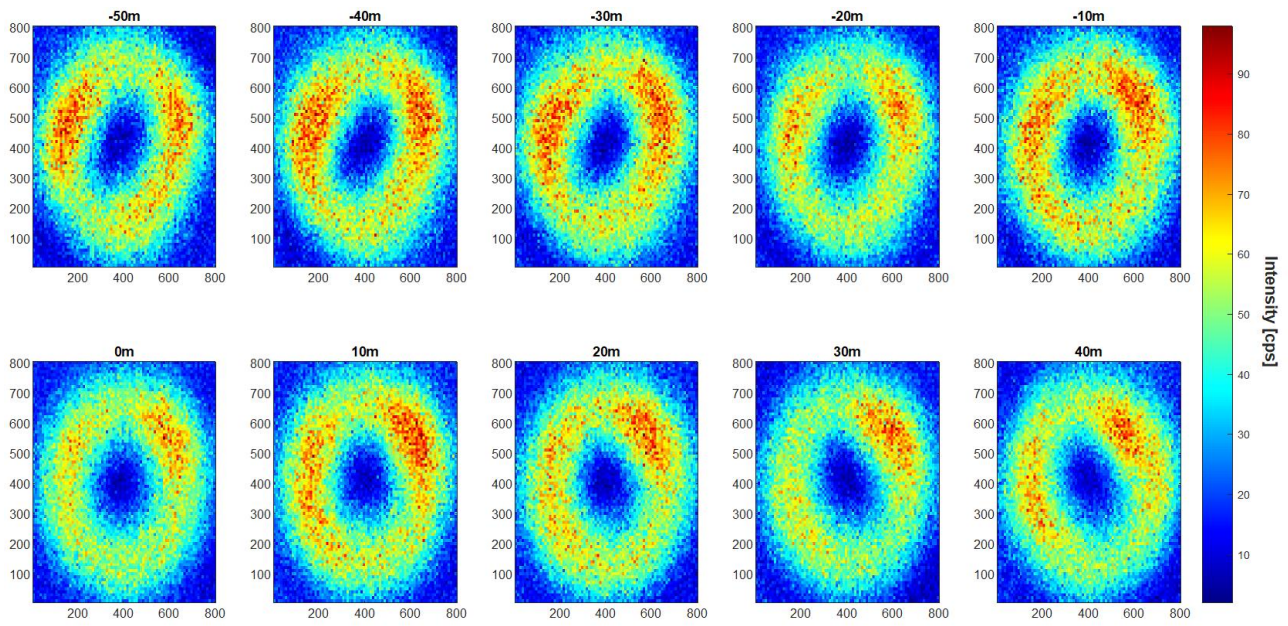


Figure IV.9: Top-hat beam under the influence of applied astigmatism in XY.

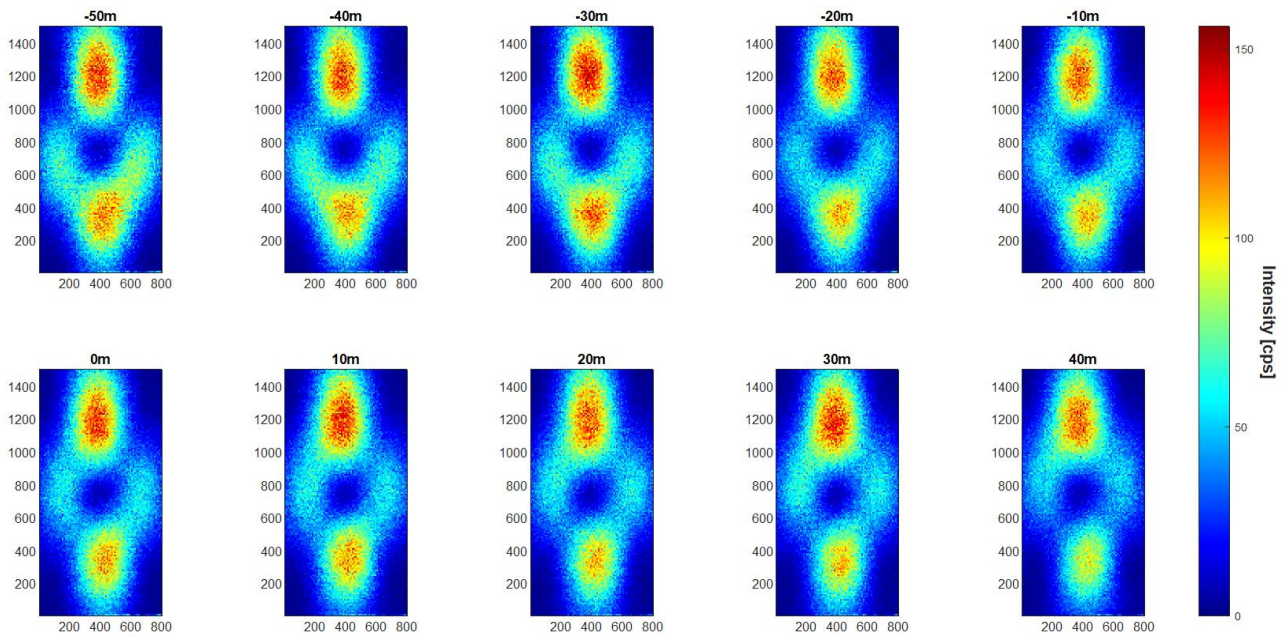


Figure IV.10: Top-hat beam under the influence of applied astigmatism in XZ.

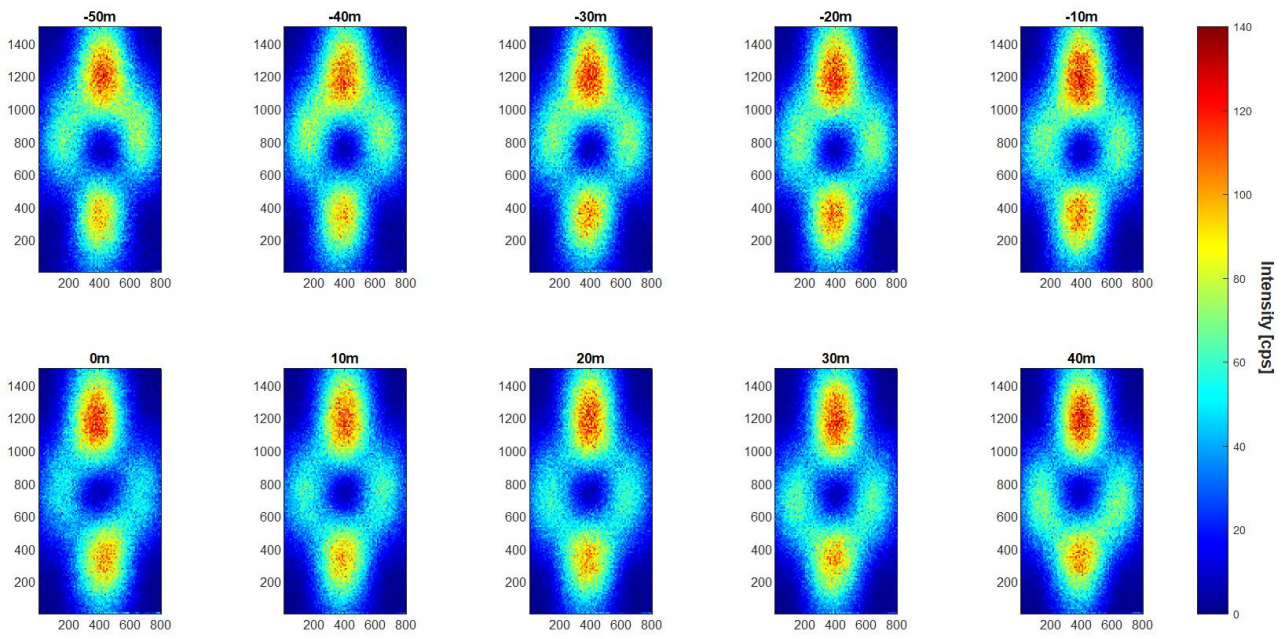


Figure IV.11: Top-hat beam under the influence of applied astigmatism in YZ.

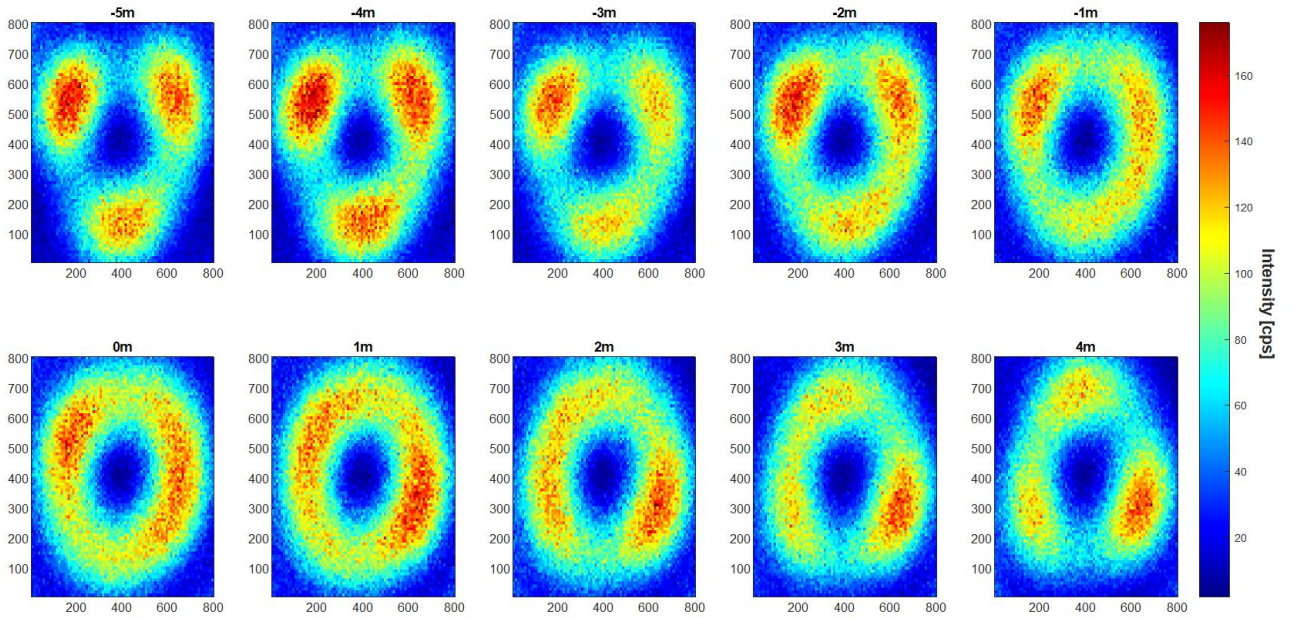


Figure IV.12: Top-hat beam under the influence of applied trefoil in XY.

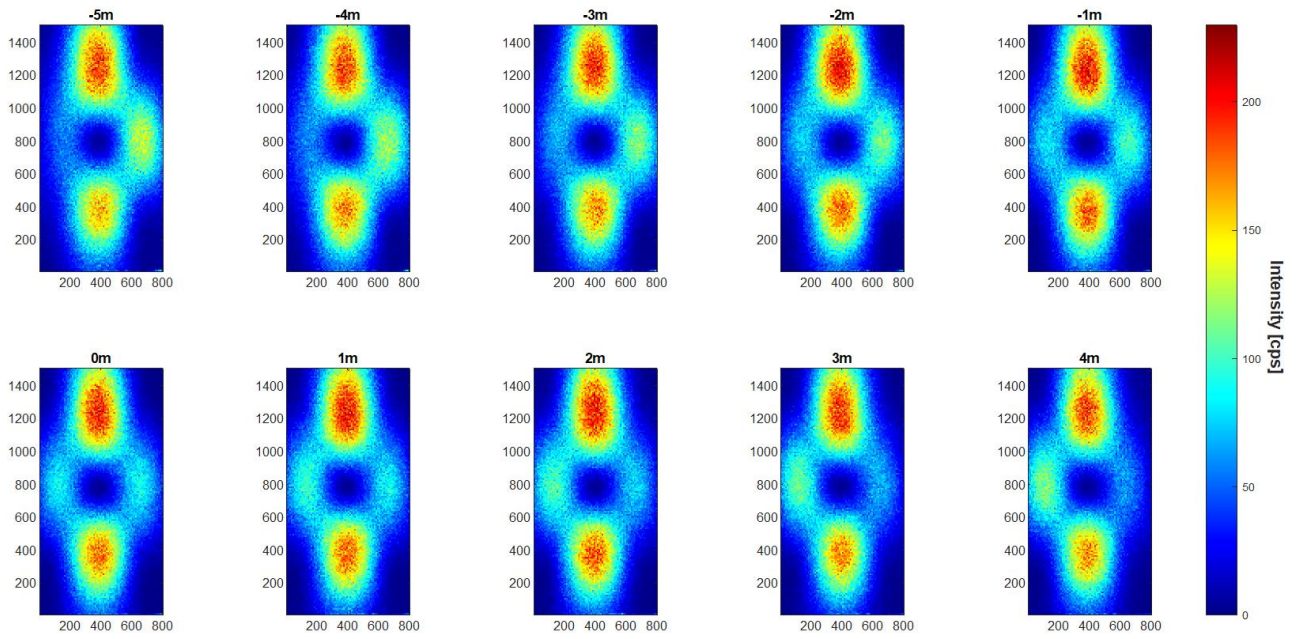


Figure IV.13: Top-hat beam under the influence of applied trefoil in XZ.

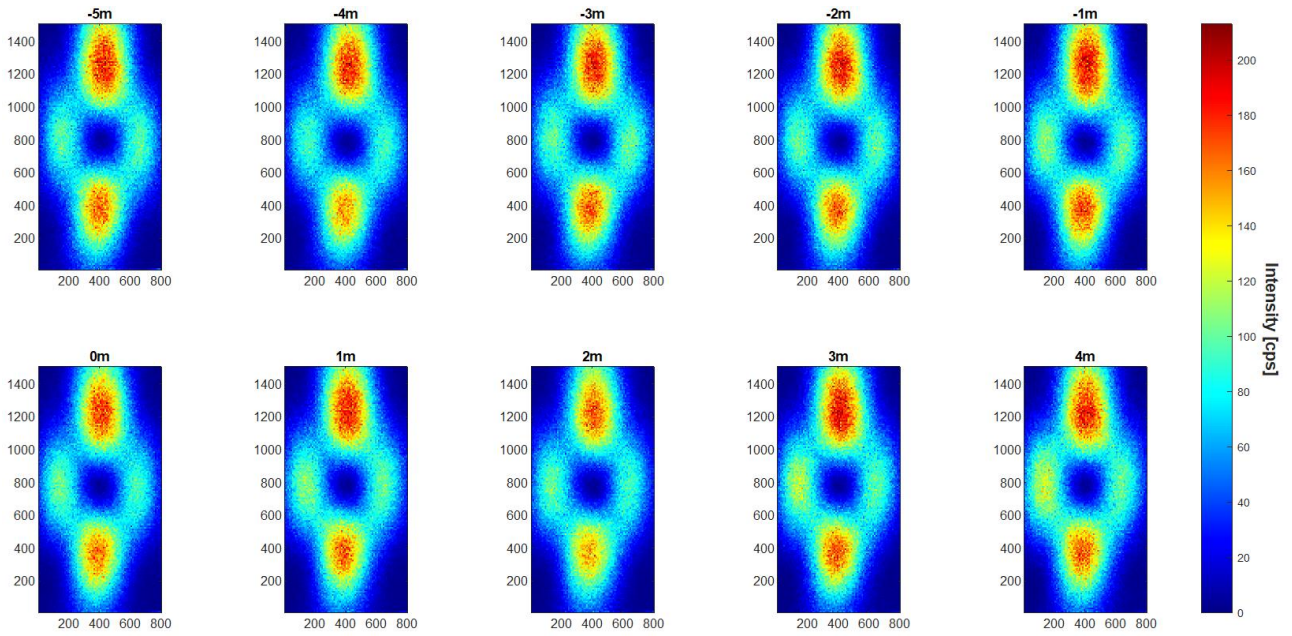


Figure IV.14: Top-hat beam under the influence of applied trefoil in YZ.

V. Discussion

The master thesis project effectively demonstrated the effectiveness of Python's implementation of an indirect sensing approach using pupil segmentation to mitigate optical aberrations. The implementation significantly enhanced the quality of the vortex and top-hat beams' shapes, which are of utmost importance for the imaging and tracking capabilities at the subnanometric scale of the *MINFLUX* superresolution microscopy technique.

By using a *LC-SLM* to systematically introduce controlled phase variations across the segmented portions of the objective lens, the implementation leveraged the interference patterns produced by the interaction of central and segmented electric fields with different phases when scanning fluorescent beads, sequentially. This data-driven approach enabled the extraction of phase information, which underwent a series of processing steps, including phase unwrapping, polynomial fitting, interpolation, and extrapolation. These steps collectively yielded to phase maps that were uploaded into *the LC-SLM* to correct aberrations within the wavefront, as shown in Figure IV.5 and Figure IV.6.

Moreover, the project included deliberately inducing controlled aberrations onto the beam profiles after the corrections (Figures 7-14) to corroborate the effects on the beam quality shown in the simulations presented in Figure II.9 and Figure.10. The studied aberrations were astigmatism and trefoil, while induced coma beams were omitted experimentally due to an error in the coma definition on the *LC-SLM*.

Notably, the effect of the aberrations on the experimental beams exhibits the same behavior as shown in the simulations (considering the case of high aberration magnitudes), with the highlight that the studied aberrations exhibited symmetry around their zero magnitude values but with a change in direction.

For the vortex beam, oblique astigmatism was found to introduce asymmetry into the pattern, resulting in substantial distortion, as seen in Figure IV.7. This distortion led to the splitting of the vortex beam into two distinct parts, accompanied by a tilted and stretched central hollow. On the other hand, the trefoil effect was identified to contribute significantly to the formation of a complex, distorted pattern characterized by a distinctive three-lobe shape, as displayed in Figure IV.8.

In the XY plane (Figure IV.9), when subjected to oblique astigmatism, the top-hat profile assumed an elliptical shape with distinct radii along the x and y directions. These differing radii correspond to varying focal lengths in their respective dimensions. In the XZ and YZ planes, astigmatism introduced elongation of the intensity profile along the Y and X axes, as shown in Figure IV.10 and Figure IV.11, respectively.

Conversely, when considering trefoil along the y-axis, the top-hat profile exhibits three lobes in both the XY and XZ planes, displayed in Figure IV.12 and Figure IV.13, respectively. This arrangement gives rise to triangular-like intensity distributions akin to those encountered with the vortex beam. However, in contrast to its effect on the XY and YZ planes, trefoil has minimal impact on the YZ plane, preserving the intensity distribution as seen in Figure IV.14.

While the pupil segmentation technique with the interpolation approach has proven effective in the correction process, it is imperative to explore alternative methods for both phase extraction and aberration correction due to the limitations of the current approach.

One notable limitation is the long acquisition time associated with the pupil segmentation technique. The process takes approximately 12s for every recorded interference intensity profile between the central pupil

field and the field of each pupil. Considering that four images are recorded for every central-pupil pair (50 in total), the acquisition time is around 2400s (≈ 40 min).

Another limitation is the presence of aberration effects even after correction. An example of residual aberration can be observed in Figure IV.7, where remnants of astigmatism and trefoil are evident in the top-hat beam profile across the XY plane. This indicates that the current technique might not be entirely successful in eradicating aberrations, which can be attributed to the interpolation approach since the entirety of the pupil space is not covered when segmenting it.

Therefore, alternatives that use of the entirety of the pupil space, avoiding the need of using interpolation methods as in the pupil segmentation approach, are of interest for future optical aberration correction implementations, such as the dynamic adaptive scattering compensation holography *DASH* algorithm from [34]. Additionally, the study could also be extended to characterize the residual aberrations for manual fine-tuning after the correction is performed and to quantify how the quality of the zero in the vortex and top-hat beams degrades in the presence of these remaining aberrations.

VI. Bibliography

- [1] F. Balzarotti et al., “Nanometer resolution imaging and tracking of fluorescent molecules with minimal photon fluxes,” *Science*, vol. 355, no. 6325, pp. 606–612, Feb. 2017. doi:10.1126/science.aak9913
- [2] K. C. Gwosch et al., “Miniflux nanoscopy delivers 3D multicolor nanometer resolution in cells,” *Nature Methods*, vol. 17, pp. 217–224, Feb. 2020. doi:10.1038/s41592-019-0688-0
- [3] P. R. Krishna and D. K. Sagar, “Aberrations in theories of Optical Aberrations,” *IOSR Journal of Applied Physics*, vol. 09, no. 04, pp. 37–43, Sep. 2017. doi:10.9790/4861-0904013743
- [4] K. Niu and C. Tian, “Zernike polynomials and their applications,” *Journal of Optics*, no. 24, Nov. 2022. doi:10.1088/2040-8986/ac9e08
- [5] K. M. Hampson et al., “Adaptive optics for high-resolution imaging,” *Nature Reviews Methods Primers*, vol. 1, no. 1, 2021. doi:10.1038/s43586-021-00066-7
- [6] M. Booth, “A basic introduction to adaptive optics for Microscopy,” AO microscopy, <https://aomicroscopy.org/ao-basic-introduction> (accessed May 17, 2023).
- [7] A. Jullien, “Spatial light modulators,” *Photoniques*, no. 101, pp. 59–64, 2020. doi:10.1051/photon/202010159
- [8] A. Rennie, “The Rayleigh Criterion for microscope resolution,” *Edinburgh Instruments*, <https://www.edinst.com/ko/news/the-rayleigh-criterion-for-microscope-resolution/> (accessed May 7, 2023).
- [9] S. Dunst and P. Tomancak, “Imaging flies by fluorescence microscopy: Principles, technologies, and applications,” *Genetics*, vol. 211, no. 1, pp. 15–34, 2018. doi:10.1534/genetics.118.300227
- [10] K. Prakash, B. Diederich, R. Heintzmann, and L. Schermelleh, “Super-resolution microscopy: A brief history and new avenues,” *Philosophical Transactions of the Royal Society A: Mathematical, Physical and Engineering Sciences*, vol. 380, no. 2220, Feb. 2022. doi:10.1098/rsta.2021.0110
- [11] N. A. Jensen et al., “Coordinate-targeted and coordinate-stochastic super-resolution microscopy with the reversibly switchable fluorescent protein Dreiklang,” *ChemPhysChem*, vol. 15, no. 4, pp. 756–762, Feb. 2014. doi:10.1002/cphc.201301034
- [12] Z. Wu, X. Xu, and P. Xi, “Stimulated emission depletion microscopy for biological imaging in four dimensions: A Review,” *Microscopy Research and Technique*, vol. 84, pp. 1947–1958, Mar. 2021. doi:10.1002/jemt.23750
- [13] J. Kwon et al., “Resolft nanoscopy with photoswitchable organic fluorophores,” *Scientific Reports*, vol. 5, Dec. 2015. doi:10.1038/srep17804
- [14] H. Zhong, “Photoactivated localization microscopy (PALM): An optical technique for achieving ~10-nm resolution,” *Cold Spring Harbor Protocols*, vol. 2010, no. 12, Dec. 2010. doi:10.1101/pdb.top91

- [15] J. Xu, H. Ma, and Y. Liu, "Stochastic Optical Reconstruction Microscopy (STORM)," *Current Protocols in Cytometry*, vol. 81, Jul. 2017. doi:10.1002/cpcy.23
- [16] D. Nieves, K. Gaus, and M. Baker, "DNA-based super-resolution microscopy: DNA-paint," *Genes*, vol. 9, no. 12, p. 621, Dec. 2018. doi:10.3390/genes9120621
- [17] J. Cnossen et al., "Localization microscopy at doubled precision with patterned illumination," *Nature Methods*, vol. 17, no. 1, pp. 59–63, Dec. 2019. doi:10.1038/s41592-019-0657-7
- [18] L. Gu et al., "Molecular resolution imaging by Repetitive Optical Selective Exposure," *Nature Methods*, vol. 16, no. 11, pp. 1114–1118, Sep. 2019. doi:10.1038/s41592-019-0544-2
- [19] L. Reymond et al., "Simple: Structured illumination based point localization estimator with enhanced precision," *Optics Express*, vol. 27, no. 17, p. 24578, Aug. 2019. doi:10.1364/oe.27.024578
- [20] P. Jouchet, C. Poüs, E. Fort, and S. Lévêque-Fort, "Time-modulated excitation for enhanced single-molecule localization microscopy," *Philosophical Transactions of the Royal Society A: Mathematical, Physical and Engineering Sciences*, vol. 380, no. 2220, Feb. 2022. doi:10.1098/rsta.2020.0299
- [21] K. C. Gwosch, "Nanometer resolution imaging with minimal fluorescence photon fluxes," dissertation, 2017
- [22] K. Peng, X. Shen, and F. Huang, "Vortex beam generation method based on spatial light modulator," *IOP Conference Series: Earth and Environmental Science*, vol. 440, no. 4, p. 042082, 2020. doi:10.1088/1755-1315/440/4/042082
- [23] C. Osseforth, J. R. Moffitt, L. Schermelleh, and J. Michaelis, "Simultaneous dual-color 3D sted microscopy," *Optics Express*, vol. 22, no. 6, p. 7028, 2014. doi:10.1364/oe.22.007028
- [24] Z. Zhang et al., "Three-dimension resolution enhanced microscopy based on parallel detection," *Applied Sciences*, vol. 11, no. 6, p. 2837, 2021. doi:10.3390/app11062837
- [25] C. He et al., "Effects of optical aberrations on localization of Minflux Super-Resolution Microscopy," *Optics Express*, vol. 30, no. 26, Dec. 2022. doi:10.2139/ssrn.4160506
- [26] "LabVIEW," National Instruments, <https://www.ni.com/de-at/shop/labview.html> (accessed Aug. 4, 2023).
- [27] A. Passera. "Fiducial Bead Samples Preparation Guide," *Research Institute of Molecular Pathology*, 2023.
- [28] "MATLAB," MathWorks, <https://www.mathworks.com/products/matlab.html> (accessed Aug. 4, 2023).
- [29] "Welcome to Python," Python.org, <https://www.python.org/> (accessed Aug. 4, 2023).
- [30] Microsoft, "Visual studio code - code editing. redefined," RSS, <https://code.visualstudio.com/> (accessed Aug. 4, 2023).

- [31] M. Leutenegger, M. Geissbuehler, I. Märki, R. A. Leitgeb, and T. Lasser, "Fast focus field calculations," SPIE Digital Library, <https://nanophotonics.spiedigitallibrary.org/conference-proceedings-of-spie/6861/68610R/Fast-focus-field-calculations/10.1117/12.763188.full> (accessed Jul. 10, 2023).
- [32] P. Gao, B. Prunsche, L. Zhou, K. Nienhaus, and G. U. Nienhaus, "Background suppression in fluorescence nanoscopy with stimulated emission double depletion," *Nature Photonics*, vol. 11, no. 3, pp. 163–169, Jan. 2017. doi:10.1038/nphoton.2016.279
- [33] "Inspector," Abberior Instruments, <https://inspector.abberior-instruments.com/> (accessed Aug. 1, 2023).
- [34] M. A. May, K. K. Kummer, M. Kress, M. Ritsch-Marte, and A. Jesacher, "Fast holographic scattering compensation for deep tissue biological imaging," *Biophotonics Congress 2021*, 2021. doi:10.1364/ntm.2021.ntu1c.1

Appendix A - Complementary Information

A.1. Generalized MINFLUX statistics

In section II.5.1, a concise explanation was provided to highlight the rationale behind the ability to adjust the photon efficiency in the MINFLUX localization principle using a 1D example. However, for a comprehensive and quantitative analysis that encompasses various dimensions, beam shapes, and the number of exposures, a suitable statistical description is required.

If a single fluorescent emitter at a position $\bar{r}_m \in \mathbb{R}^d$ in a d dimensional space is exposed to K spatially different light intensities $\{I_0(\bar{r}), I_1(\bar{r}), \dots, I_{K-1}(\bar{r})\}$, a photon collection $\bar{n} = \{n_0, n_1, \dots, n_{K-1}\}$ will be detected. The detected number of photons n_i from each exposure I_i follow a Poisson distribution with mean λ_i . In the scenario when the saturation of the emitter and detector are avoided, with negligible dark counts from the detector and background (denoted by $^{(0)}$), the mean λ_i of the Poisson distribution can be approximated to [21]

$$\lambda_i^{(0)}(\bar{r}_m) = c_e q_e \sigma_a I_i(\bar{r}_m) \quad (\text{A.1})$$

where c_e represents the detection efficiency of the system, q_e the quantum yield, σ_a the absorption cross-section of the emitter at the illumination's wavelength I_i . Assuming that background and dark counts contributions follow Poisson distributions, the mean of their distributions $\lambda_i^{(b)}$ in exposure i can be summed up to the mean from the detected number of photons n_i distribution and still result in a Poisson distribution with mean [21]

$$\lambda_i(\bar{r}_m) = \lambda_i^{(0)}(\bar{r}_m) + \lambda_i^{(b)}(\bar{r}_m) \quad (\text{A.2})$$

The study can be conducted with a fixed total number N of photons without any loss in generalizability

$$N = \sum_{i=0}^{K-1} n_i \quad (\text{A.3})$$

and n_i following the Poisson distribution

$$P(n_i) \sim \text{Poisson}(\lambda_i) = \frac{\lambda_i^{n_i} e^{-\lambda_i}}{n_i!} \quad \forall i \in [0, 1, \dots, K-1] \quad (\text{A.4})$$

the joint probability distribution $P(\bar{n}|N)$ for n_i conditioned to a total of N detected photons is given by a multinomial distribution

$$P(\bar{n}|N) = \frac{N!}{\prod_{i=0}^{K-1} n_i!} \prod_{j=0}^{K-1} p_j^{n_j} \quad (\text{A.5})$$

where the multinomial parameter p_i takes the form

$$p_i(\bar{r}_m) = \frac{\lambda_i}{\sum_{j=0}^{K-1} \lambda_j} = \frac{\lambda_i^{(0)} + \lambda_i^{(b)}}{\sum_{j=0}^{K-1} (\lambda_j^{(0)} + \lambda_j^{(b)})} \quad \text{with } i \in [0, 1, \dots, K-1] \quad (\text{A.6})$$

The number of independent photon counts n_i and multinomial parameters p_i are reduced from K to $K-1$; the $K-1$ dimensional space is referred to as the *reduced \bar{p} -space* and allows to rewrite equation 3.21 as

$$P(\bar{n}|N) = \frac{N!}{\prod_{i=0}^{K-1} n_i!} \left(\prod_{i=0}^{K-2} p_i^{n_i} \right) \left(1 - \sum_{j=0}^{K-2} p_j \right)^{n_{K-1}} \quad (\text{A.7})$$

The definition of signal-to-background ratio (*SBR*) is the following

$$SBR(\bar{r}_m) = \frac{\sum_{i=0}^{K-1} \lambda_i^{(0)}(\bar{r}_m)}{\sum_{j=0}^{K-1} \lambda_j^{(b)}(\bar{r}_m)} \approx \frac{c_e q_e \sigma_a \sum_{i=0}^{K-1} I_i(\bar{r}_m)}{\sum_{j=0}^{K-1} \lambda_j^{(b)}(\bar{r}_m)} \quad (\text{A.8})$$

This allows equation A.6 to be rewritten as

$$\begin{aligned} p_i(\bar{r}_m) &= \frac{SBR(\bar{r}_m)}{SBR(\bar{r}_m) + 1} \frac{\lambda_i^{(0)}(\bar{r}_m)}{\sum_{j=0}^{K-1} \lambda_j^{(0)}(\bar{r}_m)} + \frac{1}{1 + SBR(\bar{r}_m)} \frac{\lambda_i^{(b)}(\bar{r}_m)}{\sum_{j=0}^{K-1} \lambda_j^{(b)}(\bar{r}_m)} \\ &\approx \frac{SBR(\bar{r}_m)}{SBR(\bar{r}_m) + 1} \frac{I_i(\bar{r}_m)}{\sum_{j=0}^{K-1} I_j(\bar{r}_m)} + \frac{1}{1 + SBR(\bar{r}_m)} \frac{\lambda_i^{(b)}(\bar{r}_m)}{\sum_{j=0}^{K-1} \lambda_j^{(b)}(\bar{r}_m)} \end{aligned} \quad (\text{A.9})$$

Equation A.9 can be further simplified assuming that the background signal is the same for all exposures, i.e., the background contribution is independent of the individual illuminations $I_i(\bar{r})$ ($\lambda_i^{(b)} = \lambda_j^{(b)}$)

$$p_i(\bar{r}_m) \approx \frac{SBR(\bar{r}_m)}{SBR(\bar{r}_m) + 1} p_i^{(0)}(\bar{r}_m) + \frac{1}{1 + SBR(\bar{r}_m)} \frac{1}{K} \quad (\text{A.10})$$

where K represents the number of exposures and $p_i^{(0)}(\bar{r}_m)$ the component i of the parameter vector \bar{p} ; if the negligible background is considered, the emitter brightness cancels out :

$$p_i^{(0)}(\bar{r}_m) = \frac{\lambda_i^{(0)}}{\sum_{j=0}^{K-1} \lambda_j^{(0)}} \approx \frac{I_i(\bar{r}_m)}{\sum_{j=0}^{K-1} I_j(\bar{r}_m)} \quad \text{with } i \in [0, 1, \dots, K-1] \quad (\text{A.11})$$

Furthermore, calculating the Fisher information and the corresponding Cramér-Rao bound (CRB) is a method that allows to the extent to which the MINFLUX localization scheme enhances the information about the emitter's spatial location [21].

The Fisher information $\mathcal{F}_{\bar{\theta}}$ is a measurement of the amount of information content that an (observable) random variable vector \bar{X} holds on the parameter vector $\bar{\theta}$ of a model distribution of \bar{X} . If the likelihood function is given by $\mathcal{L}(\bar{\theta}|\bar{X})$, the Fisher information takes the form

$$(\mathcal{F}_{\bar{\theta}})_{ij} = E_{\bar{\theta}} \left[\left(\frac{\partial}{\partial \theta_i} \ln(\mathcal{L}(\bar{\theta}|\bar{X})) \right) \cdot \left(\frac{\partial}{\partial \theta_j} \ln(\mathcal{L}(\bar{\theta}|\bar{X})) \right) \right] \quad (\text{A.12})$$

where $E_{\bar{\theta}}[\dots]$ represents the expectation value with respect to $\bar{\theta}$. The inverse of the Fisher information allows to obtain the Cramér-Rao bound $\Sigma_{CRB}(\bar{\theta})$

$$\Sigma_{CRB}(\bar{\theta}) = \mathcal{F}_{\bar{\theta}}^{-1} \quad (\text{A.13})$$

As per the Cramér-Rao inequality, the lower bound for the covariance of any unbiased estimator \bar{U} , which estimates the parameters $\bar{\theta}$ of the distribution of \bar{X} , is provided by the CRB.

$$\text{cov}_{\bar{\theta}}(\bar{U}(\bar{X})) \geq \Sigma_{CRB}(\bar{\theta}) \quad (\text{A.14})$$

where the matrix inequality $\text{cov}_{\bar{\theta}}(\bar{U}(\bar{X})) \geq \Sigma_{CRB}(\bar{\theta})$ represents the condition where the matrix $\text{cov}_{\bar{\theta}}(\bar{U}(\bar{X})) - \Sigma_{CRB}(\bar{\theta})$ is positive semidefinite.

In the MINFLUX scheme, the observable random variable \bar{X} is represented by the detected photon counts $\bar{n} = \{n_0, n_1, \dots, n_{K-1}\}$ and $\bar{\theta}$ is represented by the multinomial parameter vector \bar{p} (equation 3.22), therefore, the Fisher information in equation A.12 takes the form

$$(\mathcal{F}_{\bar{p}})_{ij} = E_{\bar{p}} \left[\left(\frac{\partial}{\partial p_i} \ln(\mathcal{L}(\bar{p}|\bar{n})) \right) \cdot \left(\frac{\partial}{\partial p_j} \ln(\mathcal{L}(\bar{p}|\bar{n})) \right) \right] \quad (\text{A.15})$$

The conditioned joint probability distribution $P(\bar{n}|\bar{p})$ defined in equation 3.23 gives the likelihood function $\mathcal{L}(\bar{p}|\bar{n})$ for having the parameter vector \bar{p} in the measured set of photons \bar{n} as follows

$$\mathcal{L}(\bar{p}|\bar{n}) = P(\bar{n}|\bar{p}, N) = \frac{N!}{\prod_{i=0}^{K-1} n_i!} \left(\prod_{i=0}^{K-2} p_i^{n_i} \right) \left(1 - \sum_{j=0}^{K-2} p_j \right)^{n_{K-1}} \quad (\text{A.16})$$

The Fisher information expression can be further simplified considering a Kronecker delta function δ_{ij} and the total number of photons N

$$(\mathcal{F}_{\bar{p}})_{ij} = N \left(\frac{1}{p_{K-1}} + \delta_{ij} \frac{1}{p_i} \right) \quad \text{with } i, j \in [0, 1, \dots, K-2] \quad (\text{A.17})$$

By employing the Jacobian matrix \mathcal{J}^* , the Fisher information $\mathcal{F}_{\bar{p}}$ with respect to the parameter vector \bar{p} undergoes a variable transformation to consider the emitter position \bar{r}_m instead

$$\mathcal{F}_{\bar{r}_m} = \mathcal{J}^{*T} \mathcal{F}_{\bar{p}} \mathcal{J}^* \quad (\text{A.18})$$

where $\mathcal{J}^* \in \mathbb{R}^{(K-1) \times d}$ is the reduced Jacobian matrix for the variable transformation to the reduced \bar{p} -space from the \bar{r}_m -space:

$$(\mathcal{J}^*)_{ij} = \frac{\partial p_i}{\partial r_j} \quad (\text{A.19})$$

Applying the transformation equation A.18 on equation A.17, as well as considering

$$\sum_{i=0}^{K-2} \frac{\partial p_i}{\partial r_j} = \frac{\partial}{\partial r_j} \sum_{i=0}^{K-2} p_i = \frac{\partial}{\partial r_j} (1 - p_{K-1}) = \frac{\partial p_{K-1}}{\partial r_j} \quad (\text{A.20})$$

The Fisher information $\mathcal{F}_{\bar{r}_m}$ is then derived

$$\mathcal{F}_{\bar{r}_m} = N \sum_{i=0}^{K-1} \frac{1}{p_i} \begin{pmatrix} \left(\frac{\partial p_i}{\partial r_{m_1}} \right)^2 & \frac{\partial p_i}{\partial r_{m_1}} \frac{\partial p_i}{\partial r_{m_2}} & \dots & \frac{\partial p_i}{\partial r_{m_1}} \frac{\partial p_i}{\partial r_{m_d}} \\ \frac{\partial p_i}{\partial r_{m_2}} \frac{\partial p_i}{\partial r_{m_1}} & \left(\frac{\partial p_i}{\partial r_{m_2}} \right)^2 & \dots & \frac{\partial p_i}{\partial r_{m_2}} \frac{\partial p_i}{\partial r_{m_d}} \\ \vdots & \vdots & \ddots & \vdots \\ \frac{\partial p_i}{\partial r_{m_d}} \frac{\partial p_i}{\partial r_{m_1}} & \frac{\partial p_i}{\partial r_{m_d}} \frac{\partial p_i}{\partial r_{m_2}} & \dots & \left(\frac{\partial p_i}{\partial r_{m_d}} \right)^2 \end{pmatrix} \quad (\text{A.21})$$

The lower bound on the achievable localization precision for any unbiased position estimator described by the CRB can then be determined from equation A.13

$$\Sigma_{CRB}(\bar{\Theta}) = \mathcal{F}_{\bar{r}_m}^{-1} \quad (\text{A.22})$$

The square root of the arithmetic mean of the eigenvalues σ_i of $\Sigma_{CRB}(\bar{\Theta})$, which will be used in further analysis, can also be determined as follows

$$\sigma_{CRB}(\bar{r}_m) = \sqrt{\frac{1}{d} \text{tr}(\Sigma_{CRB}(\bar{r}_m))} \quad (\text{A.23})$$

where d represents the number of dimensions of \bar{r}_m and $\text{tr}(\dots)$ a trace operator, equivalent to the norm $\phi[\mathcal{F}]$ for the Fisher information matrix

$$\phi[\mathcal{F}] = \left(\frac{\text{tr}(\mathcal{F}^q)}{d} \right)^q \quad (\text{A.24})$$

Furthermore, Isotropy \mathbb{I} can also be defined

$$\mathbb{I} = \sqrt{\frac{\min_{i \in [1, \dots, d]} \sigma_i(\bar{r}_m)}{\max_{i \in [1, \dots, d]} \sigma_i(\bar{r}_m)}} \quad (\text{A.25})$$

A.2. Focus field package calculations

The plane wave spectrum *PWS* technique stands as an established and efficient strategy for modeling the behavior of electromagnetic *EM* fields in terms of propagation and diffraction. Its effectiveness arises from its ability to transition *EM* fields from one plane to another using the computational speed of the fast Fourier transform *FFT* [31].

In the realm of microscopy, this foundational concept underpins the Debye approximation, serving as a versatile means to implement the Debye integral. This implementation considers the combined effects of amplitude, phase, and polarization in a comprehensive manner. Particularly suitable for streamlined numerical assessment, this approach significantly reduces the computational load required to calculate the amplitude, phase, and polarization of an *EM* distribution engendered by a microscope objective with high numerical aperture *NA* [31].

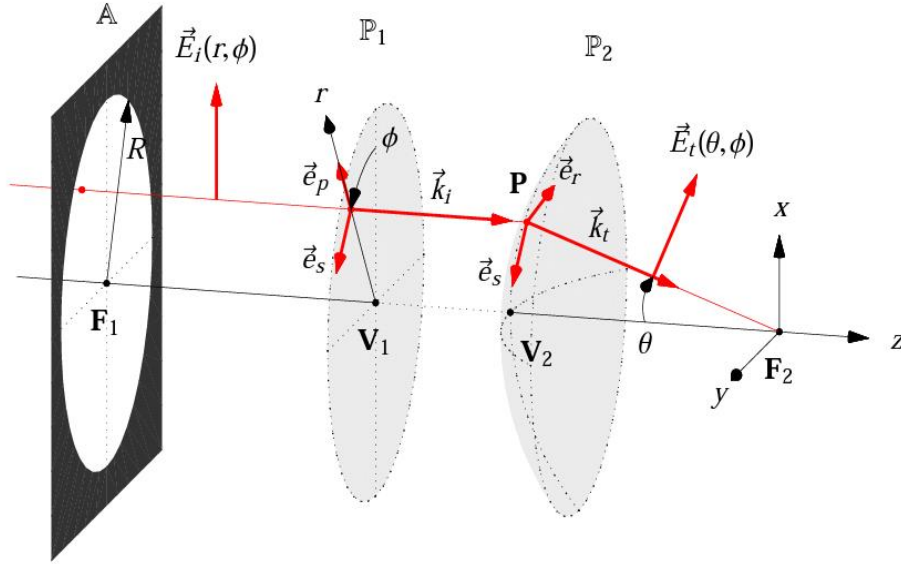


Figure A.1: Optical setup in focus field simulations: The aperture stop *A*, characterized by a radius *R*, represents the objective. The principal planes \mathbb{P}_1 and \mathbb{P}_2 , marked by vertex points V_1 and V_2 , and foci F_1 and F_2 , respectively [31]

Considering a coherent and monochromatic wave field oriented parallel to the optical axis. This wave field traverses the aperture stop *A*, progresses towards the principal plane \mathbb{P}_1 , and subsequently advances to the principal plane \mathbb{P}_2 . Upon arrival at \mathbb{P}_2 , the wave field experiences refraction, leading it to converge and focus at the focal point F_2 . A point labeled *P*, situated on the principal plane \mathbb{P}_2 , serves as a demonstration of how a ray is concentrated at \mathbb{P}_2 , guiding it towards the focal point F_2 . The spherical surface \mathbb{P}_2 is centered on F_2 , and the angular deviation θ at point *P* is determined by [31]

$$\sin \theta = \frac{r NA}{R n_t} \quad (\text{A.26})$$

In equation A.26, *r* represents the off-axis coordinate of the incident wave, *R* represents the radius of the aperture stop, *NA* stands for the numerical aperture of the objective, and n_t indicates the refractive index behind the surface \mathbb{P}_2 . In this considered setup, the aperture *A* is located in the back focal plane, creating a telecentric imaging system.

Typically, pupils are used to simulate wave propagation within the objective instead of principal planes. However, when directly transitioning the incident wave from the entrance pupil to the exit pupil, accounting for diffraction at the aperture stop within the objective becomes more intricate. In this context, the wave's progression from the aperture plane A to the principal plane $\mathbb{P}1$ can be effectively computed using the *PWS* method or, in many cases, by applying conventional principles of Fourier optics [31].

The incident field $\vec{E}_i(r, \phi)$ at $\mathbb{P}1$ is decomposed into two constituents: a radial component (p-polarized) and a tangential component (s-polarized). The vectors corresponding to p-polarization and s-polarization are...

$$\vec{e}_p = \begin{pmatrix} \cos \phi \\ \sin \phi \\ 0 \end{pmatrix} \text{ and } \vec{e}_s = \begin{pmatrix} -\sin \phi \\ \cos \phi \\ 0 \end{pmatrix} \quad (\text{A.27})$$

where ϕ denotes the azimuth angle revolving around the z-axis. After transmission, the unit vector \vec{e}_p undergoes deflection by an angle θ and becomes.

$$\vec{e}_r = \begin{pmatrix} \cos \phi \cos \theta \\ \sin \phi \cos \theta \\ \sin \theta \end{pmatrix} \quad (\text{A.28})$$

Therefore, the amplitude, phase, and polarization of the transmitted field at $\mathbb{P}2$ is

$$\vec{E}_t(\theta, \phi) = t_p(\vec{E}_i \cdot \vec{e}_p)\vec{e}_r + t_s(\vec{E}_i \cdot \vec{e}_s)\vec{e}_s \quad (\text{A.29})$$

The transmission coefficients, labelled as $t_p(\theta, \phi)$ and $t_s(\theta, \phi)$, quantify how much of the incident field is transmitted through a system, accounting for elements such as the pupil function and apodization for p-polarization and s-polarization, respectively. These coefficients encapsulate both the phase aberrations and amplitude changes (attenuations) occurring at point $\mathbb{P}2$ in a comprehensive manner [31].

In the context of a paraxial incident field (near the optical axis), any axial component E_{iz} is considered negligible when compared to the lateral components E_{ix} and E_{iy} , even if the incident phase varies. In the Debye approximation, the transmitted field vector E_t can be conceptualized as the collection of plane wave spectra constituting the focused field vector E near $F2$. Consequently, the electric field vector E at a specific point (x, y, z) is derived by integrating the propagated plane waves [31].

$$\vec{E}(x, y, z) = \frac{-if}{\lambda_0} \int_0^\theta \sin \theta \int_0^{2\pi} \vec{E}_t(\theta, \phi) e^{i(k_{zz}z - k_x x - k_y y)} d\phi d\theta \quad (\text{A.30})$$

The factor $e^{ik_{zz}z}$ takes into consideration the phase change as the wave propagates along the z-axis, while the term $e^{-i(k_x x + k_y y)}$ accounts for the phase difference of the wavefront at points (x, y, z) of the central axis in comparison to the point $(0, 0, z)$ on the central axis. The integration covers the solid angle Ω over which the observation at point $\mathbb{P}2$ is made from the point $F2$, where $\sin(\theta) = NA/n_t$. The wave vector k_t is then represented in spherical coordinates (θ, ϕ) by [31]

The factor $e^{ik_{zz}z}$ considers the phase alteration as the wave propagates along the z-axis, while the term $e^{-i(k_x x + k_y y)}$ accommodates the phase distinction of the wavefront at coordinates (x, y, z) along the central axis when compared to the point $(0, 0, z)$ on the same axis. The integration encompasses the solid angle Ω , representing the field of view at point $\mathbb{P}2$ from the standpoint of $F2$. Here, $\sin(\theta) = NA/n_t$, where NA is the numerical aperture and n_t is the refractive index. The wave vector k_t is subsequently expressed in spherical coordinates (θ, ϕ) as follows [31].

$$\vec{k}_t(\theta, \phi) = k_0 n_t \begin{pmatrix} -\cos \phi \sin \theta \\ -\sin \phi \sin \theta \\ \cos \theta \end{pmatrix} \quad \text{where } k_0 = \frac{2\pi}{\lambda_0} \quad (\text{A.31})$$

To calculate Equation A.30, direct numerical integration considering the coordinate transformations involved is the common approach. This process leads to the Richard-Wolf integral representation. However, an alternative approach for sampling $a(\theta, \phi)$ is employed. This approach maintains a constant value of $d\Omega = \sin\theta d\theta d\phi$ by using $\cos\theta_m = 1 - m\Delta\theta$, with $m \in \mathbb{N}$. The sampling grid can be defined by varying values of m belonging to the set $\{1 \text{ to } M\}$, and n belonging to the set $\{1 \text{ to } N\}$.

$$\theta_m = \arccos\left(1 - m \frac{1 - \sqrt{1 - NA^2/n_t^2}}{M}\right) \quad \text{and } \phi_n = \left(n - \frac{1}{2}\right) \frac{2\pi}{N} \quad (\text{A.32})$$

When considering $\theta=0$, a weighting of sampling point $d\Omega = \pi\theta^2/4$ is introduced. While the goal is to decrease the number of sampling points along θ , it's feasible to amalgamate the computation of the integrand with its integration into a single matrix multiplication, resulting in better computational efficiency. The procedure described for evaluating the Debye diffraction integral in Equation A.30 is notably swift, albeit still slower in comparison to the conventional calculation of a Fraunhofer diffraction integral. However, Equation A.30 can be easily reformulated as a Fourier transform. This transform is accomplished by breaking down the phase factor into lateral and axial components and then performing the integration over $\mathbb{P}1$ instead of $\mathbb{P}2$. By leveraging Equations A.1 and A.6, the integration step $d\Omega$ for a sample over $\mathbb{P}2$ is projected onto $\mathbb{P}1$, yielding the subsequent outcome [31].

$$d\Omega = \left(\frac{NA}{Rn_t}\right)^2 \frac{rdrd\phi}{\cos\theta} = \left(\frac{NA}{Rn_t}\right)^2 \frac{dxdy}{\cos\theta} = \frac{1}{k_t^2} \frac{dk_x dk_y}{\cos\theta} \quad (\text{A.33})$$

Considering the sampling approach into equation A.30 leads to

$$\vec{E}(x, y, z) = \frac{-if}{\lambda_0 k_t^2} \iint_{r < R} \vec{E}_t(\theta, \phi) e^{ik_z z / \cos\theta} e^{-i(k_x x + k_y y)} dk_x dk_y \quad (\text{A.34})$$

Expanding the integration over (k_x, k_y) across the entire \mathbb{R}^2 space by imposing $|E_t| = 0$ for distances beyond R , which allows the Debye diffraction integral as a Fourier transform of the weighted field E_t

$$\vec{E}(x, y, z) = \frac{-if}{\lambda_0 k_t^2} \mathcal{F}(\vec{E}_t(\theta, \phi) e^{ik_z z / \cos\theta}) \quad (\text{A.35})$$

To numerically implement Equation A35, a *FFT* is employed on the field weighted at $\mathbb{P}2$. The numerical computation uses equidistant sampling of k_x and k_y , with intervals denoted as $\Delta K = \Delta K = k_0 NA/M$. As consequence, there are M sampling points spanning the aperture radius, thereby determining the distribution of sampling points on $\mathbb{P}2$ [31].

$$\theta_{mn} = \arcsin\left(\frac{\Delta K}{k_t} \sqrt{m^2 + n^2}\right) \quad \text{and } \phi_{mn} = \arctan\left(\frac{n}{m}\right) \quad \text{for } [m], [n] \leq M \quad (\text{A.36})$$

Considering the integration step $(\Delta K)^2$ with Equation A.35 leads to the numerical implementation in the focus field Python package:

$$\vec{E}(x_{kl}, y_{kl}, z) = \frac{-iR^2}{\lambda_0 f M^2} \text{FFT}(e^{ik_z m n z} \vec{E}_t(\theta_{mn}, \phi_{mn}) / \cos\theta_{mn}) \quad (\text{A.37})$$

A.3. Sample preparation

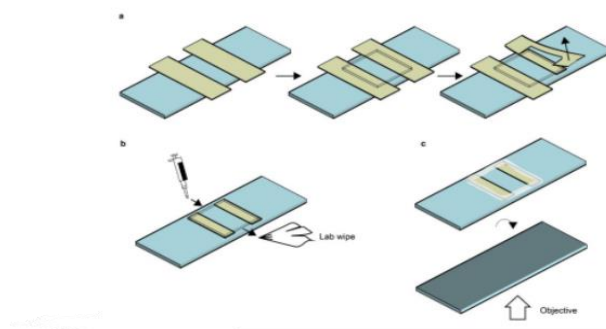


Figure A.2: Chamber slide and gold fiducials [27]

Samples for *PSF* measurements were prepared by setting up a flow chamber using a clean coverslip (Figure A.2). The coverslip was securely positioned in either a Teflon box or racks to maintain stability during experiments. To prevent leakage, Scotch tape was used to seal the coverslip effectively. The chamber's volume ranged from 10 to 20 μl , carefully controlled to optimize conditions for calculations and maintain consistent sample sizes across experiments.

The first step in sample preparation was the dilution of 90 nm gold nanoparticles (AuNPs) obtained from Cytodiagnosics, which were stored in the fridge at 4°C. The dilution was carried out at a ratio of 1:5, meaning that 1 part of the AuNPs was mixed with 4 parts of 1xPBS (Phosphate-Buffered Saline Solution), resulting in a 5-fold reduction in the concentration of AuNPs.

Before proceeding with the incubation, it was important to address the issue of sedimentation, which commonly occurred with the AuNPs. To resuspend the nanoparticles uniformly, the liquid in the bottle was gently swirled without causing any agitation or bubble formation. This step ensured that the AuNPs were well-dispersed and evenly distributed within the solution.

The incubation of the AuNPs solution within the flow chamber lasted for 5 minutes. To introduce the solution into the chamber, a pipette tip was positioned close to the entrance, and a gentle pushing motion was applied. This allowed the liquid to seep between the coverslip and slide, effectively filling the flow chamber.

For bubbles, if movable, they were gently pushed out. Non-moving bubbles were considered non-interfering. Some bubbles near the end were removed by suctioning from the opposite side, connecting them to the outside air, and then flushing liquid from the opposite direction.

After incubation, a washing step was performed on the flow chamber using 20 μl of 1xPBS. This process included gently pushing out the liquid while touching the opposite end with a Kimwipe. The Kimwipe was used to absorb and replace the liquid within the chamber, all done with care to maintain a steady flow and prevent bubbles. To ensure skill in this step, practice runs were conducted with water in an empty chamber before the actual experiments.

In addition to the AuNPs, 100 nm TetraSpeck beads were used as part of the experiments. The TetraSpeck beads were combined with the gold nanoparticles at a dilution ratio of 1:250 in 1xPBS. To ensure proper dispersion, the mixture of AuNPs and TetraSpeck beads was sonicated for 15 minutes.

Appendix B - Attributions and Approvals

B.1. Copyright clearance for non-self-produced figures

- **Figure II.1 [4]**

TOPICAL REVIEW • OPEN ACCESS
Zernike polynomials and their applications
Kuo Niu^{1,2}  and Chao Tian^{3,1,2} 
Published 15 November 2022 • © 2022 The Author(s). Published by IOP Publishing Ltd
[Journal of Optics Volume 24 Number 12](#)
Citation Kuo Niu and Chao Tian 2022 *J. Opt.* 24 123001
DOI 10.1088/2040-8986/ac9e08

 Original content from this work may be used under the terms of the Creative Commons Attribution 4.0 licence. Any further distribution of this work must maintain attribution to the author(s) and the title of the work, journal citation and DOI.

2040-8986/22/123001+54\$33.00 Printed in the UK © 2022 The Author(s). Published by IOP Publishing Ltd

- **Figure II.2[7]**

Spatial light modulators

Aurélie Jullien*

Institut de Physique de Nice, Valbonne, France

* e-mail: aurelie.jullien@inphyni.cnrs.fr

Abstract

Spatial Light Modulators (SLMs) are quasiplanar devices, allowing for the modulation of the amplitude, phase and polarization, or a combination of these parameters of an incident light beam according to the two spatial dimensions of the modulator. SLMs are employed in many different fields and are the subject of continuous technological development.

© The authors, published by EDP Sciences, 2020

 This is an Open Access article distributed under the terms of the Creative Commons Attribution License (<http://creativecommons.org/licenses/by/4.0/>), which permits unrestricted use, distribution, and reproduction in any medium, provided the original work is properly cited.

- **Figure II.3 and Figure II.4 [9]**



[Genetics](#), 2019 Jan; 211(1): 15–34.

Published online 2018 Nov 26. doi: [10.1534/genetics.118.300227](https://doi.org/10.1534/genetics.118.300227)

PMCID: PMC6325693

PMID: [30626639](https://pubmed.ncbi.nlm.nih.gov/30626639/)

Imaging Flies by Fluorescence Microscopy: Principles, Technologies, and Applications

[Sebastian Dunst](#)^{1,1} and [Pavel Tomancak](#)^{1,1}

• [Author information](#) • [Article notes](#) • [Copyright and License information](#) • [Disclaimer](#)

[Copyright](#) © 2019 Dunst and Tomancak

Available freely online through the author-supported open access option. This is an open-access article distributed under the terms of the Creative Commons Attribution 4.0 International License (<http://creativecommons.org/licenses/by/4.0/>), which permits unrestricted use, distribution, and reproduction in any medium, provided the original work is properly cited.

- Figure II.5, Figure II.6 and Figure II.7 [1]

THE AMERICAN ASSOCIATION FOR THE ADVANCEMENT OF SCIENCE LICENSE TERMS AND CONDITIONS

Jul 31, 2023

This Agreement between Politecnico di Torino -- Francisco Matos ("You") and The American Association for the Advancement of Science ("The American Association for the Advancement of Science") consists of your license details and the terms and conditions provided by The American Association for the Advancement of Science and Copyright Clearance Center.

License Number	5599281377037
License date	Jul 31, 2023
Licensed Content Publisher	The American Association for the Advancement of Science
Licensed Content Publication	Science
Licensed Content Title	Nanometer resolution imaging and tracking of fluorescent molecules with minimal photon fluxes
Licensed Content Author	Francisco Balzarotti, Yvan Eilers, Klaus C. Gwosch, Arvid H. Gynnä, et al.
Licensed Content Date	Dec 22, 2016
Licensed Content Volume	355
Licensed Content Issue	6325
Volume number	355
Issue number	6325
Type of Use	Thesis / Dissertation
Requestor type	Scientist/individual at a research institution
Format	Electronic
Portion	Text Excerpt
Number of pages requested	2
Title	Characterization and Correction of Optical Aberrations in MINFLUX Superresolution Microscopy
Institution name	Politecnico di Torino
Expected presentation date	Aug 2023
Portions	Figure 1, Figure 2

- **Figure II.8 [22]**

PAPER • OPEN ACCESS

Vortex Beam Generation Method based on Spatial Light Modulator

Kaifei Peng¹, Xueju Shen¹ and Fuyu Huang¹

Published under licence by IOP Publishing Ltd

[IOP Conference Series: Earth and Environmental Science, Volume 440, Environmental Science and Technology](#)

Citation Kaifei Peng et al 2020 *IOP Conf. Ser.: Earth Environ. Sci.* 440 042082

DOI 10.1088/1755-1315/440/4/042082



Content from this work may be used under the terms of the [Creative Commons Attribution 3.0 licence](#). Any further distribution of this work must maintain attribution to the author(s) and the title of the work, journal citation and DOI.

- **Figure II.9 [24]**



Article

Three-Dimension Resolution Enhanced Microscopy Based on Parallel Detection

Zhimin Zhang ¹, Shaocong Liu ¹, Minfei He ¹, Yuran Huang ¹ , Cui Fang Kuang ^{1,2,3,*}, Yubing Han ¹, Xiang Hao ¹  and Xu Liu ¹



Copyright: © 2021 by the authors.
Licensee MDPI, Basel, Switzerland.
This article is an open access article distributed under the terms and conditions of the Creative Commons Attribution (CC BY) license (<https://creativecommons.org/licenses/by/4.0/>).

- **Figure A.1 [31]**

Optics Express Vol. 14, Issue 23, pp. 11277-11291 (2006) • <https://doi.org/10.1364/OE.14.011277>

Fast focus field calculations

Marcel Leutenegger, Ramachandra Rao, Rainer A. Leitgeb, and Theo Lasser

 Open Access

OPEN ACCESS LICENSES

Open Access Publishing Agreement

Our "Copyright Transfer and Open Access Publishing Agreement" (OAPA) is the default option for most authors when publishing in one of our fully open access journals or when opting for open access in our hybrid journals. All articles published under our OAPA are freely accessible, while copyright is transferred to Optica Publishing Group. Authors may post the published version of their article to their personal website, institutional repository, or a repository required by their funding agency. Authors and readers may use, reuse, and build upon the article, or use it for text or data mining, as long as the purpose is non-commercial and appropriate attribution is maintained.

B.2. Statement of non-plagiarism

I hereby declare that all information in this report has been obtained and presented in accordance with academic rules and ethical conduct and the work I am submitting in this report, except where I have indicated, is my own work.

A handwritten signature in black ink, appearing to read 'F. Matos', with a stylized flourish extending from the end.

Francisco Matos Álvarez, B.Eng.

B.3. Supervisor approval

I, the undersigned, Francisco Balzarotti, supervisor of Francisco Matos Álvarez, student of the PSRS EMJMD, during his master thesis at the Research Institute of Molecular Pathology certify that I approve the content of this master thesis report entitled '*Characterization and Correction of Optical Aberrations in MINFLUX Superresolution Microscopy*'.

A handwritten signature in black ink, consisting of a large, stylized 'F' followed by several loops and a long, sweeping tail that ends in a sharp point.

2023-08-21

Francisco Balzarotti, Ph.D.

B.4. Acknowledgement

I would like to express my heartfelt gratitude to the academic consortium of the Erasmus Mundus Joint Master Degree in Photonics for Security Reliability and Safety (PSRS), with the invaluable support provided by the Erasmus+ Programme of the European Union. This program has not only provided me with a world-class education but has also enriched my academic journey in immeasurable ways.

I am deeply thankful to the professors, mentors, and all the staff members associated with the PSRS program for their unwavering dedication to fostering excellence in education, especially my academic supervisors *Nathalie Destouches* (Université Jean Monnet), *Jyrki Saarinen* (University of Eastern Finland), *Amine Nait-Ali* (Université Paris-Est Créteil), and *Carlo Ricciardi* (Politecnico di Torino).

I am extremely grateful to *Francisco Balzarotti*, Group Leader at the Research Institute of Molecular Pathology in Vienna, for offering me the invaluable opportunity to join his team during my master's thesis project. This project allowed me to immerse myself in the realm of superresolution microscopy, undeniably motivating me to further explore this field in a future PhD.

The completion of my project would not have been possible without the guidance of my mentor, *Alba Gómez-Segalas*, and her consistent provision of constructive feedback. I would also like to extend my gratitude to my fellow teammates for their encouragement: *Maximilian Geismann*, *Mehrta Shirzadian Yazd*, *Alessandro Passera*, *Jakub Dokulil*, *Simon Roschger*, and *Anna Deputatova*.

Over the past two years, a rollercoaster of emotions and experiences unfolded, with both highs and lows. Through it all, I'm grateful that I was never alone, as I found companionship and friendship accounting for countless cherished moments with my fellow classmates, especially *Héctor Jair Morales*, *Alberto Otero Casado*, *Iye Szin Ang*, *Fernando Diego Engels Crespo*, and *Zachary Labossiere*.

I cannot begin to express my appreciation to my friends from Panama: *Yarubby Mc Naughton*, *Lizeth Medina*, *José and Max Hylton*, who despite the distance have consistently stayed connected and encouraged me to continue even when the path seemed impossible. I will always be grateful for their presence in my life.

I am truly grateful for the love and support from my parents, *Francisco Matos Castillo* and *Marlene Álvarez Sánchez*, along with my sister *Stephanie Mabel Matos Álvarez*. However, it was my grandmother, *Felicia de Matos Castillo*, the one who truly made me be the person I am today. Her belief in me, even in the face of challenges, has been the driving force behind my perseverance and accomplishments my whole life. May she rest in peace.

From the bottom of my heart, I am extremely grateful to my Swedish partner, *Simon Marcus Åkesson*. He has been not only a companion during the last year but a true source of strength, I am truly lucky to have him by my side. Here's to the chapters we've written together and the ones that lie ahead, Jag älskar dig.

Francisco Matos
Vienna, August 21st, 2023